Applied Thermal Engineering 302 (2026) 131923

Contents lists available at ScienceDirect

Applied Thermal Engineering

journal homepage: www.elsevier.com/locate/ate

Research Paper

Assessment of key performance indicators for a reciprocating compressor with electronically controlled vapor injection

Luigi Fusco [a], Giulio Lenzi [b], Michele Manno [a,*], Stefano Mazzoni [a]

[a] University of Rome Tor Vergata, Via del Politecnico, 1, Rome, 00133, Italy
[b] Officine Mario Dorin spa, Via Aretina, 388, Compiobbi (FI), 50061, Italy

ARTICLE INFO

Keywords:
Reciprocating compressor
Isentropic and volumetric efficiency
CO_2 transcritical cycle
Voorhees cycle
Vapor injection
Heat pump

ABSTRACT

This study develops a comprehensive and physically consistent mathematical model of a reciprocating compressor with vapor injection (VI) to be used in a CO_2 transcritical cycle (Voorhees cycle), removing the constant-volume mixing assumption adopted in a previous work. The formulation accounts for coupled thermodynamic and fluid-dynamic interactions, heat transfer and leakage correlations, and flexible vapor injection enabled by solenoid valve technology. The parameters required by the model are identified by validating the reference model without vapor injection against experimental data. After validation, the model was used to assess key performance indicators of the VI compressor under a wide range of operating conditions, namely isentropic efficiency, suction volumetric efficiency, and a novel injection volumetric efficiency that specifically describes the injection phase. At the compressor level, the injection pressure and the injection valve opening time can be set independently, and increasing either reduces the specific work, which is lowered by up to 14.1 % under favorable conditions; the compressor-level optimum is thus reached at high injection pressure and long valve opening time. At the cycle level, however, these two variables are coupled by the steady-state mass balance of the flash tank, so that the optimum shifts to low injection pressure and long valve opening time, the condition that maximizes the injected mass available from the flash expansion.

1. Introduction

Decarbonization represents a fundamental challenge for the energy sector, particularly in the context of space and process heating, which accounts for a considerable share of global greenhouse gas emissions [1,2]. Electrification of heating demand through high-efficiency technologies such as heat pumps (HPs) is widely regarded a strategic pathway to reduce carbon intensity in residential and industrial applications [3,4]. Despite their proven energy performance, large-scale HP deployment is still constrained by high upfront costs, technical barriers, and regulatory uncertainties [1,5]. Furthermore, the environmental impact of working fluids has become a critical research focus, following international agreements such as the Montreal Protocol and its successive amendments, which first targeted substances with high Ozone Depletion Potential (ODP) and then hydrofluorocarbons (HFCs) due to their high Global Warming Potential (GWP) [6]. In response, research efforts are increasingly directed towards the development and assessment of low-GWP refrigerants [7]. Among these, carbon dioxide has re-emerged, based on the work of [8], as a promising candidate, particularly under transcritical operating conditions [9]. It combines favorable thermophysical properties with minimal environmental impact, especially in terms of ODP and GWP [10,11].

Since Lorentzen's studies, CO_2 has been used in numerous applications, such as heat pump water heaters [12], space heating [13], and many others [14]. Furthermore, in the field of heat pumps, a significant number of studies and research activities have been carried out to improve their performance [15–17]. In particular, several modifications to the basic cycle have been proposed [18], among which vapor injection into the compression chamber, originally introduced by Voorhees [19] with the concept of a "multiple effect" compressor [19], stands out [20]. This technique, based on the admission of vapor at an intermediate pressure during compression, reduces the specific compression work, improving the coefficient of performance (COP) [21,22]. In reciprocating compressors, vapor can be introduced into the cylinder through an admission port opened at the bottom dead center. Although this method inherently couples injected mass with operating pressures and port geometry [23], recent developments in solenoid valve technology enable more flexible control of the vapor

* Corresponding author.
E-mail addresses: luigi.fusco@alumni.uniroma2.eu (L. Fusco), g.lenzi@dorin.com (G. Lenzi), michele.manno@uniroma2.it (M. Manno), stefano.mazzoni@uniroma2.it (S. Mazzoni).

https://doi.org/10.1016/j.applthermaleng.2026.131923
Received 10 April 2026; Received in revised form 8 June 2026; Accepted 9 June 2026
Available online 13 June 2026

injection, partially decoupling the mass flow rate from the injection pressure. Consequently, the development of a detailed mathematical model becomes essential to characterize the vapor injection process in reciprocating compressors, capturing the complex interactions between mass flow dynamics, pressure variations, and thermodynamic transformations. In a previous work [24], two different layouts corresponding to the Flash-Tank Vapor Injection (FTVI) and SubCooler Vapor Injection (SCVI) Voorhees cycles were analyzed, assuming the mixing process as a constant-volume adiabatic process. However, a more comprehensive mathematical model of the reciprocating compressor can remove this assumption, allowing for a more realistic description of the in-cylinder processes during vapor injection.

Throughout the years, a variety of models have been developed to simulate reciprocating compressors in steady-state and transient regimes. These include performance-oriented models that estimate isentropic and volumetric efficiencies [25,26], simplified steady-state formulations [27], models based on polytropic transformations [28,29], and lumped-element approaches [30,31]. Among the various physical phenomena involved, heat transfer within the cylinder plays a key role, as it significantly influences both volumetric and isentropic efficiencies. In fact, as Adair et al. [32] highlighted, neglecting heat transfer can result in an overestimation of both volumetric and isentropic efficiency of approximately 10–20 % [32]. Several heat transfer correlation models have been introduced in the literature, among which two of the earliest and most influential are those by Annand [33] and Woschni [34], originally formulated for internal combustion engine applications [33,34]. In the context of reciprocating compressors, the first adaptations were also derived from these models, followed by the contribution of Adair et al. [32]. More recently, Disconzi et al. [35] and Aigner and Steinrück [36] developed correlations specifically tailored for reciprocating compressors [35,36].

Existing models of vapor-injection compressors either rely on simplified thermodynamic assumptions, such as the constant-volume or constant-pressure mixing approximations adopted in cycle-level analyses [22,24], or are semi-empirical formulations calibrated against experimental data for specific compressor types [37]. The present work differs from both classes by developing a first-principles lumped-parameter model that explicitly resolves the in-cylinder injection dynamics, including the pressure drop across the injection valve, the variable-pressure mixing inside the cylinder, heat transfer with the cylinder walls, and leakage through the piston–cylinder clearance. This allows a direct quantification of the prediction error associated with the simplified mixing assumptions, which is presented in Section 3.3.

Therefore, this study presents a comprehensive mathematical model of the reciprocating compressor, validated using experimental data supplied by the Italian manufacturer Officine Mario Dorin spa. The model was validated for the reference configuration without VI to accurately capture the operational characteristics of the reference compressor. The required model parameters, such as clearances and valve flow coefficients, were identified during this phase. Following successful validation, the model was extended to simulate a next-generation reciprocating compressor currently in development. Vapor injection was then incorporated into the model to analyze its impact and evaluate potential performance enhancements, overcoming the simplifying assumption of constant-volume mixing previously adopted [24].

Furthermore, since conventional definitions of volumetric and isentropic efficiency are formulated for compressors without vapor injection, the present study introduces revised definitions designed to accurately represent the performance characteristics of VI compressors. More specifically, different definitions of volumetric and isentropic efficiency available in the existing literature for VI compressors [37,38] are tested to identify and validate the most appropriate approaches, and new definitions (supercharging coefficient and injection volumetric efficiency) are proposed to more effectively describe the injection process.

The mathematical model is then used to evaluate the specific work required by the VI compressor, which is compared with that of the reference configuration to assess potential energy savings. Finally, an artificial neural network (ANN) was developed to rapidly assess key performance indicators of the reciprocating compressor equipped with a solenoid valve under a wide range of operating conditions and was applied to assess the performance of a transcritical heat pump equipped with a VI compressor.

The original contribution of this article can thus be summarized as follows.

- A lumped-parameter model of the VI compressor, including heat transfer and leakage effects, is developed and presented.
- Novel performance indicators (supercharging coefficient and injection volumetric efficiency) that describe more accurately the injection process are proposed.
- The reduction in specific work achievable through vapor injection is quantitatively assessed across the operating envelope.
- The relationship to the authors' previous work is clarified: by removing the constant-volume mixing assumption and resolving the injection event in time, the present model confirms the direction of the previously reported findings, corrects their magnitude (the simplified assumption overestimates the specific work by approximately 7–10.5 %), and extends them by treating the injection valve opening duration as a controllable degree of freedom.

The paper is organized as follows. Section 2 describes the mathematical model of the reciprocating compressor, including the revised definitions of volumetric and isentropic efficiencies, the analysis framework adopted for model validation, and the ANN developed. Section 3 discusses the results, starting with the validation of the mathematical model, then the numerical results obtained for volumetric efficiency, supercharging parameter, isentropic efficiency, and volumetric injection efficiency, and finally the specific work to quantify the benefits of vapor injection.

2. Methods

This section outlines the main assumptions and governing equations used in the implementation of the VI reciprocating compressor model, developed to go beyond the simplifying assumption of constant-volume mixing [24]. Vapor is assumed to be injected through a solenoid valve, which allows mass flow into the cylinder to be controlled by adjusting the valve opening time (Fig. 1(a)). In a heat pump or refrigeration system, vapor could be produced by isenthalpic expansion of the refrigerant from the gas cooler pressure to the injection pressure in the Flash-Tank Vapor Injection (FTVI) configuration represented in Fig. 1(b) [24].

Section 2.1 describes the mathematical model that represents the operation of the reciprocating compressor, while Section 2.2 introduces the definitions of the key performance indicators evaluated in this work, including revised formulations of the volumetric and isentropic efficiencies applicable to VI compressors and the newly proposed injection volumetric efficiency, supercharging coefficient, and mass discharge coefficient. Finally, Section 2.3 outlines the approach adopted for model validation, while Section 2.4 briefly describes the ANN developed to characterize the performance of VI compressors in higher level models.

2.1. Mathematical model

In order to remove the simplifying assumption of constant-volume mixing after vapor injection, a lumped-parameter model was developed to describe the thermodynamic processes taking place inside the cylinder, including the suction, discharge, and injection processes. The main assumptions underlying the model are as follows:

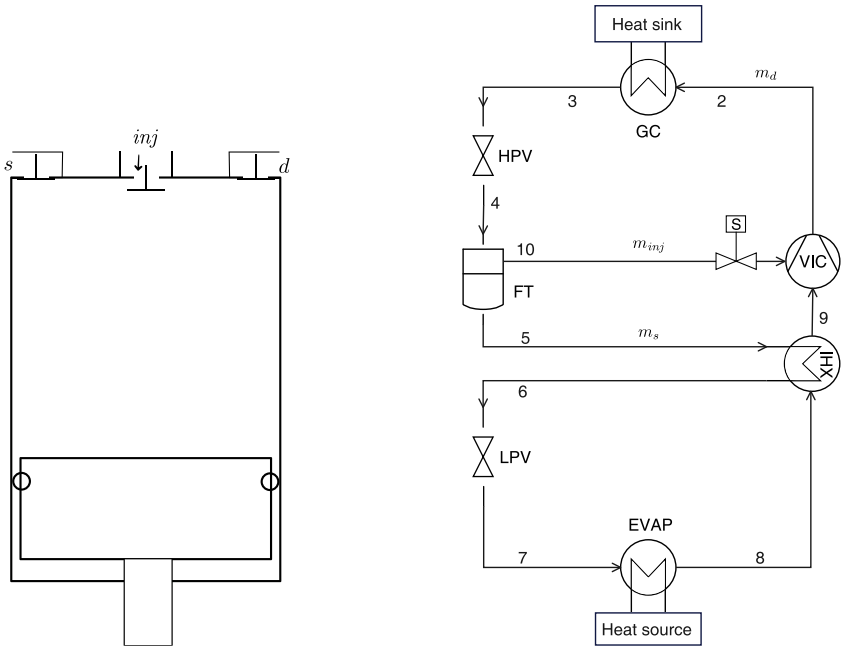

(a) VI reciprocating compressor (b) Heat pump layout

Fig. 1. Schematic representation of a heat pump with a vapor-injection compressor (VIC).

- The suction and discharge valves are automatically actuated;
- Fluid injection is performed through a solenoid-controlled injector, with the start time and opening duration treated as independent parameters;
- External heat exchange with the environment is not considered; only heat transfer between the working fluid and the cylinder walls is accounted for;
- Leakage through the clearance between the piston and the cylinder is taken into account by considering an equivalent cylinder–piston gap.

2.1.1. Kinematics

The following equations describe the evolution of the available fluid volume (V) and the piston velocity (v_p) as functions of the crank angle θ:

$$\frac{V(\theta)}{V_{dis}} = f_V(\theta) = \zeta + \frac{1}{2}\left[R + 1 - \cos(\theta) - \sqrt{R^2 - \sin^2(\theta)}\right] \tag{1}$$

$$\frac{v_p(\theta)}{\overline{v}_p} = f_{v_p}(\theta) = \frac{\pi}{2}\frac{\sin(\theta)}{1 + \cos(\theta)\sqrt{R^2 - \sin^2(\theta)}}, \tag{2}$$

where ζ represents the clearance volume ratio, R is the ratio between the connecting rod length and the crank radius, V_{dis} is the compressor displacement, and $\overline{v}_p$ is the mean piston velocity, which depends on piston stroke L and rotational speed n:

$$\overline{v}_p = 2Ln. \tag{3}$$

The crank angle θ can be used in place of time in the governing equations due to the known relationship between crankshaft rotation and time, expressed as:

$$\theta = 2\pi nt. \tag{4}$$

2.1.2. Flow through the valves

The flow through the suction and discharge valves, as well as through the injector holes, was modeled in a similar manner by evaluating the effective thermodynamic properties of the fluid. The kinetic energy of the fluid upstream of the restricted section was neglected and a discharge coefficient μ was introduced to take into account the irreversibility of the process. Denoting by the subscript $_1$ the conditions upstream of the restricted section, and by $_2$ the conditions at the restriction, the mass flow rate through the valve cross section S is obtained from the velocity at the restriction calculated from the energy conservation equation:

$$h_2 + v_2^2/2 = h_1 + v_1^2/2 \approx h_1 \tag{5}$$

$$h_2 = h_1 - \mu^2\left[h_1 - h(p_2, s_1)\right] \tag{6}$$

$$v_2 = \sqrt{2(h_1 - h_2)} = \mu\sqrt{2\left[h_1 - h(p_2, s_1)\right]} \tag{7}$$

$$\rho_2 = \rho(p_2, h_2) \tag{8}$$

$$\dot{m} = S\rho_2 v_2. \tag{9}$$

The mass drawn, discharged, and injected per cycle is the integral over the work cycle of the respective flow rates:

$$m_s = \oint \dot{m}_s \mathrm{d}t = \frac{1}{2\pi n}\oint \dot{m}_s \mathrm{d}\theta \tag{10}$$

$$m_d = \oint \dot{m}_d \mathrm{d}t = \frac{1}{2\pi n}\oint \dot{m}_d \mathrm{d}\theta \tag{11}$$

$$m_{inj} = \oint \dot{m}_{inj} \mathrm{d}t = \frac{1}{2\pi n}\oint \dot{m}_{inj} \mathrm{d}\theta. \tag{12}$$

2.1.3. Conservation equations

The mass and energy conservation equations, applied to the time-varying control volume defined by the volume available to the fluid, allow the calculation of the fluid properties within the cylinder over time:

$$\frac{\mathrm{d}(\rho V)}{\mathrm{d}t} = \dot{m}_{inj} + \dot{m}_s - \dot{m}_d \tag{13}$$

$$\frac{\mathrm{d}(\rho V u)}{\mathrm{d}t} = \dot{m}_{inj}h_{inj} + \dot{m}_s h_s - \dot{m}_d h_d + \dot{W} + \dot{Q}, \tag{14}$$

where $\dot{W}$ and $\dot{Q}$ denote the mechanical power transferred by the piston to the fluid and the rate of heat transfer between cylinder walls and fluid, respectively:

$$\dot{W} = -p(\theta)S_{cyl}v_p(\theta) \tag{15}$$

$$\dot{Q} = \alpha(\theta)A(\theta)[T_w - T(\theta)], \tag{16}$$

with $S_{cyl} = \pi D^2/4$ being the cylinder cross section, α the convective heat transfer coefficient and A the heat transfer surface, which depends on the crank angle θ, since the height of the lateral surface l varies with the position of the piston:

$$A(\theta) = 2S_{cyl} + \pi D l(\theta)\,. \tag{17}$$

Introducing the following dimensionless variables:

$$\check{p} = \rho/\rho_0, \quad \check{u} = u/u_0, \quad \check{h} = h/u_0\,, \tag{18}$$

where $\rho_0 = \rho(t = 0)$ and $u_0 = u(t = 0)$ represent the initial conditions of density and specific internal energy of the fluid, the normalized equations implemented in the model are obtained as follows:

$$\frac{\mathrm{d}\check{\rho}}{\mathrm{d}\theta} = \frac{1}{\pi f_{V(\theta)}}\left[SR_{in}\check{\rho}_{in}\frac{v_{in}}{\overline{v}_p} - SR_{out}\check{\rho}_{out}\frac{v_{out}}{\overline{v}_p} + SR_{inj}\check{\rho}_{inj}\frac{v_{inj}}{\overline{u}_p} - \check{\rho}(\theta)f_{v_p}(\theta)\right] \tag{19}$$

$$\frac{\mathrm{d}\check{u}}{\mathrm{d}\theta} = \frac{1}{\pi f_{V(\theta)}}\left[\begin{array}{l} SR_{in}\frac{\check{\rho}_{in}}{\check{\rho}(\theta)}\frac{v_{in}}{\overline{v}_p}(\check{h}_s - \check{u}(\theta)) - SR_{out}\frac{\check{\rho}_{out}}{\check{\rho}(\theta)}\frac{v_{out}}{\overline{v}_p}(\check{h}(\theta) - \check{u}(\theta)) + \\ + SR_{inj}\frac{\check{\rho}_{inj}}{\check{\rho}(\theta)}\frac{v_{inj}}{\overline{v}_p}(\check{h}_{inj} - \check{u}(\theta)) - f_{v_p}(\theta)\frac{p}{\rho u_0} + \frac{\alpha A(T_w - T)}{\rho u_0 S_{cyl}\overline{v}_p} \end{array}\right], \tag{20}$$

where SR is the ratio of the valve flow area to the cross-sectional area of the cylinder S_{cyl}, and the subscripts *in*, *out* and *inj* denote the suction, discharge and injection valves, respectively.

The last term on the right-hand side of Eq. (19) represents the effect of the volume variation on the fluid density within the cylinder. In contrast, the last two terms of Eq. (20) account for the work carried out by the piston on the fluid and the heat exchanged between the fluid and the cylinder walls, respectively. For the latter contribution, the relevant models will be described in detail in the following section. Finally, the work per cycle and the work per unit discharged mass are given by:

$$W_c = \oint \dot{W}\,\mathrm{d}t = \frac{1}{2\pi n}\oint \dot{W}(\theta)\mathrm{d}\theta\,, \tag{21}$$

$$W = W_c/m_d\,. \tag{22}$$

2.1.4. Heat transfer model

One of the primary challenges in modeling reciprocating compressors is the dynamic variability of internal processes. While the compression and re-expansion phases tend to exhibit relatively stable velocity profiles, the thermal exchanges during the suction and discharge stages are significantly influenced by the complex flow behavior through the valve system. Disconzi et al. [35] addressed this complexity by segmenting the compressor cycle into four fundamental processes, allowing a more accurate representation of the heat transfer phenomena that occur in each process [35]. The present study follows this heat transfer modeling approach, which is described in the following paragraphs. The selection of the Disconzi et al. [35] correlation [35] followed a preliminary comparative assessment with the Adair et al. [32] model [32], which is the most commonly used alternative correlation specifically developed for reciprocating compressors. The correlations originally proposed for internal combustion engines [33,34] were not considered, since the in-cylinder flow and thermal conditions of a reciprocating compressor operating on a non-reactive working fluid differ substantially from the combustion environment for which they were developed. The comparison between the Disconzi and Adair correlations was carried out by evaluating the predicted volumetric efficiency against the experimental data of the CD6-1600-72H compressor used for model validation (Section 2.3) over the clearance volume ratio range ζ = 1–5 % specified by the manufacturer. Within this range, the Adair correlation consistently overestimates the volumetric efficiency — implying an underestimation of in-cylinder heat transfer — and matches the experimental data only when ζ is extended to approximately 8 %, outside the physically meaningful range for the present compressor. This behavior is consistent with the findings of Tuhovcák et al. [39], who reported that the Adair correlation systematically underestimates in-cylinder heat transfer compared with the Disconzi correlation in reciprocating compressor applications [39]. By contrast, the Disconzi correlation provides volumetric efficiency predictions in good agreement with the experimental data within the manufacturer-specified clearance range.

Table 1
Nusselt number correlations and characteristic fluid velocity for each process of the working cycle [35].

Process	Nusselt	Characteristic velocity
Compression	$\mathrm{Nu} = 0.08\,\mathrm{Re}^{0.8}\,\mathrm{Pr}^{0.6}$	$v_c = v_{p,corr}$
Discharge	$\mathrm{Nu} = 0.08\,\mathrm{Re}^{0.8}\,\mathrm{Pr}^{0.6}$	$v_c = v_{p,corr} + v_{p,corr}^{0.8} v_f^{0.2}$
Expansion	$\mathrm{Nu} = 0.12\,\mathrm{Re}^{0.8}\,\mathrm{Pr}^{0.6}$	$v_c = v_{p,corr}$
Suction	$\mathrm{Nu} = 0.08\,\mathrm{Re}^{0.9}\,\mathrm{Pr}^{0.6}$	$v_c = v_{p,corr} + 2v_{p,corr}^{-0.4} v_f^{1.4}$

The convective heat transfer coefficient α, appearing in the rightmost term of Eq. (20), is calculated as:

$$\alpha = \mathrm{Nu}\,\lambda/D\,, \tag{23}$$

where λ is the fluid conductivity. The Nusselt number Nu depends on the Reynolds and Prandtl numbers according to the following correlation:

$$\mathrm{Nu} = a\,\mathrm{Re}^b\,\mathrm{Pr}^c\,. \tag{24}$$

The values of a, b and c depend on the process within the compressor cycle and are provided in Table 1 [35]. The Reynolds number is calculated as $\mathrm{Re} = \rho v_c D/\mu$, with the characteristic velocity v_c depending on the corrected piston velocity $v_{p,corr}$ and the gas exchange velocity v_f (Table 1). According to Disconzi et al. [35], the corrected piston velocity to be used in the evaluation of Re is related to the mean piston velocity $\overline{v}_p = 2Ln$ as follows :

$$v_{p,corr} = 2\pi\overline{v}_p = 2L\omega\,, \tag{25}$$

where ω is the angular speed in rad/s [35]; the gas exchange velocity, which captures the influence of mass flow through the suction and discharge valves [39], is calculated as follows:

$$v_f = \frac{\dot{m}(t)}{\rho(t)S_{cyl}}\,. \tag{26}$$

Another important consideration concerns the mean wall temperature T_w. In this study, for simplicity, a uniform average wall temperature was assumed throughout the cylinder, without distinguishing between different regions. Since the cylinder is not equipped with an external cooling circuit, the wall temperature naturally reaches a thermal equilibrium condition over the cycle; accordingly, T_w was determined as the value yielding zero net heat transfer between the gas and the cylinder wall over the entire cycle, consistent with the assumptions described in Section 2.1. This condition was found using an iterative procedure implemented in Matlab. It is acknowledged that the assumption of spatial uniformity is a simplification, as local wall temperatures may vary between the valve region and the cylinder liner; however, for the purposes of a lumped-parameter model, this approach is considered appropriate and consistent.

2.1.5. Leakage model

A relevant source of thermodynamic inefficiency is gas leakage through the clearance between the piston and the cylinder [40]. It is well established in the literature that this leakage can reduce both the isentropic and volumetric efficiencies by approximately 2–5 % for small reciprocating compressors [41]. Gas leakage through the piston–cylinder clearance has been investigated in several studies [42–44]; in the present work, the leakage model proposed by Zuk and Smith [43]

Table 2
Inputs, parameters, and outputs of the lumped-parameter compressor model. Values of the identified parameters are determined by the validation procedure of Section 3.1 and reported in Table 8.

Quantity	Symbol	Unit	Value/Range	Source
Operating-condition inputs				
Suction pressure	p_s	MPa	function of T_{ev}	Tables 6, 4, 9
Discharge pressure	p_d	MPa	8–15	Tables 6, 4, 9
Injection pressure ratio	β_{inj}	–	1.05–1.7	Table 6
Evaporating temperature	T_{ev}	°Celsius	−20–5	Tables 6, 9
Injection valve opening	$\Delta\theta_{inj}$	°	25–40	Table 6
Geometric and kinematic parameters (manufacturer specifications)				
Stroke	L	mm	52 (CD6), 65 (CD8)	manufacturer
Bore	D	mm	58 (CD6), 65 (CD8)	manufacturer
Number of cylinders	N_{cyl}	–	6 (CD6), 8 (CD8)	manufacturer
Rotational speed	n	rpm	1450	manufacturer
Connecting rod/crank ratio	R	–	4.83 (CD6), 6.36 (CD8)	manufacturer
Suction valve area ratio	SR_s	–	9.29 % (CD6), 15.3 % (CD8)	manufacturer
Discharge valve area ratio	SR_d	–	5.71 % (CD6), 9.28 % (CD8)	manufacturer
Injection valve area ratio	SR_{inj}	–	7.7 %	Section 3.1, design
Parameters identified by model validation				
Clearance ratio	ζ	–	identified	Section 3.1, Table 8
Equivalent piston–cylinder gap	g	μm	identified	Section 3.1, Table 8
Suction valve flow coefficient	μ_s	–	identified	Section 3.1, Table 8
Discharge valve flow coefficient	μ_d	–	identified	Section 3.1, Table 8
Injection valve flow coefficient	μ_{inj}	–	0.6 (conservative)	Section 3.1
Model outputs				
Suction mass flow rate	$\dot{m}_s$	kg/s	from Eq. (43)	–
Injected mass flow rate	$\dot{m}_{inj}$	kg/s	from Eq. (44)	–
Discharge mass flow rate	$\dot{m}_d$	kg/s	from Eq. (45)	–
Discharge specific enthalpy	h_d	J/kg	from Eq. (46)	–
Mechanical power	P	W	from Eq. (47)	–
Specific work	W	kJ/kg	Eq. (22)	–
Suction volumetric efficiency	$\eta_{v,s}$	–	Eq. (28)	–
Injection volumetric efficiency	$\eta_{v,inj}$	–	Eq. (32)	–
Supercharging coefficient	χ	–	Eq. (33)	–
Mass discharge coefficient	$\lambda_{v,d}$	–	Eq. (34)	–
Isentropic efficiency	η_{is}	–	Eq. (39)	–

is adopted. This model assumes compressible, viscous, and isothermal flow between parallel plates. The compressible formulation has been selected because recent studies indicate that it provides a more accurate representation of the leakage flow under typical operating conditions. According to this model, the leakage mass flow rate can then be expressed as:

$$\dot{m}_l = \frac{\pi D g^3 p \rho}{24 \mu l}\left(1 - \frac{p_s^2}{p^2}\right), \tag{27}$$

where p, ρ, and μ are the pressure, density, and viscosity within the cylinder, respectively, and g represents the piston–cylinder clearance.

2.1.6. Numerical implementation

Table 2 summarizes the inputs, the fixed parameters, and the outputs of the lumped-parameter compressor model presented in this section. The parameters listed under "geometric and kinematic parameters" are taken directly from the manufacturer's specifications and are identical for the two compressors considered in this work (CD6-1600-72H and CD8-3000-150H, distinguished by the corresponding values in the table). The four parameters listed under "parameters identified by model validation" (the clearance ratio ζ, the equivalent piston–cylinder gap g, and the suction and discharge valve flow coefficients μ_s and μ_d) are not directly available from manufacturer specifications and are determined by a Pareto-based optimization procedure described in Section 3.1; their identified values are reported in Table 8. The injection valve flow coefficient μ_{inj} is set to a conservative value of 0.60, as discussed in Section 3.1.

The dynamic model described in this section results in a system of Ordinary Differential Equations (ODEs), and the solution procedure consists of the following steps. For a given set of operating-condition inputs and a guess of the mean wall temperature T_w, the system of Eqs. (19)–(20) is integrated over a sufficient number of compressor cycles for the cyclic state to stabilize, by means of the Matlab `ode23t` solver, which implements a Trapezoidal Rule-Extended Backward Differentiation Formula (TR-BDF2) semi-implicit method that relies on an implicit–explicit approach to solve stiff differential equations [45], with a maximum integration step of $\Delta\theta_{\max} = 0.1\,\mathrm{deg}$, chosen to resolve the valve-opening transients. At each integration step, the constitutive relations for valve flow (Eqs. (5)–(9)), in-cylinder heat transfer (Eqs. (23)–(26) and Table 1), and piston–cylinder leakage (Eq. (27)) are evaluated algebraically as functions of the instantaneous state. After each completed cycle, the net heat transferred between the working fluid and the cylinder wall is computed and used to update T_w in a fixed-point iteration, which converges when the net heat transfer over the cycle is zero. The integrated state at convergence yields the per-cycle quantities of interest (mass flow rates, specific work, and mechanical power) from which the key performance indicators of Section 2.2 are computed.

2.2. Definition of the key performance indicators

Because the injection valve is electronically controlled, the injected mass can be varied through the valve opening duration largely independently of the operating pressures; characterizing the VI compressor therefore requires, in addition to the efficiencies used for conventional machines, indicators that isolate the injection process and respond to this further control degree of freedom. The suction volumetric and isentropic efficiencies, adapted here from non-injecting compressors, describe the overall behavior of the machine and enable a direct comparison with the reference configuration, but they do not, on their own, characterize the injection process; for this reason two dedicated indicators are introduced, the injection volumetric efficiency, Eq. (32),

and the supercharging coefficient, Eq. (33), the former quantifying how effectively the valve admits mass into the cylinder relative to an upstream-state reference, and the latter the resulting enhancement of the discharged mass flow at fixed boundary pressures. As shown in Section 3.2, the proposed injection volumetric efficiency is nearly independent of the overall pressure ratio and thus describes the injection process specifically, in contrast to the existing definitions that conflate it with the overall compression.

Well-established definitions of these efficiencies exist for standard reciprocating compressors, but no standardized or widely accepted definitions are available for compressors with vapor injection; the remainder of this section therefore defines each indicator in turn, beginning with the efficiencies adapted from conventional machines and proceeding to the dedicated injection indicators. With regard to volumetric efficiency, the conventional definition can still be applied, but in this work it is labeled as *suction volumetric efficiency* $\eta_{v,s}$:

$$\eta_{v,s} = \frac{m_s}{\rho_s V_{dis}} . \tag{28}$$

However, it becomes necessary to introduce an additional efficiency metric to fully describe the performance of reciprocating compressors with vapor injection. To this end, the *injection volumetric efficiency* $\eta_{v,inj}$ is introduced [38]:

$$\eta_{v,inj} = m_{inj}/m_{inj,id} , \tag{29}$$

where the numerator represents the actual injected mass, while the denominator corresponds to the mass that could be injected into the cylinder in an ideal process. This last term could be defined as follows:

$$m_{inj,id} = \left(V_{start/end,inj}\rho_{mix}\right) - m_{s,ref/inj} . \tag{30}$$

It should be noted that this parameter was indicated as volumetric admission efficiency by Lambers [38] due to the different nature of the process, which relied on the automatic opening of an admission port by the piston as it reached the bottom dead center [38]. To assess and use the injection volumetric efficiency, it is necessary to define the ideal injected mass unequivocally: to that end, different conditions can be considered. The definitions proposed by Lambers [38] were based on knowledge of the drawn mass, which can be evaluated in a process with or without injection, and the reference volume, which can be evaluated at the beginning or end of the injection process. A summary of the different options that can be considered for the definition of injection volumetric efficiency is provided in Table 3. The main drawback of these options is the need to rely on the constant-volume mixing assumption, which makes it impossible to immediately find the injected mass from the injection volumetric efficiency and the thermodynamic states of the fluid drawn and injected into the cylinder. For this reason, in the present work, the authors propose an alternative formulation of injection volumetric efficiency, which allows for a more practical operational definition. The reference equation remains Eq. (29); however, the key difference lies in the new expression adopted for the denominator. In this regard, the ideal injected mass is defined as follows:

$$m_{inj,id} = \left(\rho_{inj} - \rho_s\right) V_{dis} . \tag{31}$$

Physically, $\rho_{inj}V_{dis}$ represents the mass that would occupy the compressor displacement volume if it were entirely filled with fluid at the upstream injection-line state, and $\rho_s V_{dis}$ the corresponding mass at the upstream suction-line state; their difference, $\left(\rho_{inj} - \rho_s\right) V_{dis}$, therefore, represents the maximum additional mass that could theoretically be added to the cylinder by injection if its content were ideally replaced by injection-state fluid. This is a thermodynamic reference for normalization, in the same spirit as the ideal suction mass $\rho_s V_{dis}$ adopted in the conventional definition of volumetric efficiency, Eq. (28). The choice of ρ_{inj} follows the same logic used for the suction process: just as Eq. (28) employs the suction-line density rather than the in-cylinder density at bottom dead center, which is affected by clearance re-expansion, valve pressure losses and wall heat transfer, and is therefore not known a priori, the injection-line density is the natural upstream reference for the injection process. Conversely, the in-cylinder density reached when the cylinder pressure equals p_{inj} would depend on the temperature attained after the irreversible mixing, on the instantaneous mass ratio and on heat transfer during injection, none of which can be determined from the compressor geometry and the upstream thermodynamic states alone; adopting it as a reference would make the efficiency definition recursive, since the outcome of the process would be required to evaluate its efficiency. The use of V_{dis} rather than the volume at the start or end of injection follows from the same reasoning: V_{dis} is a fixed geometric property of the compressor, whereas the start- and end-of-injection volumes vary with the injection valve operating parameters and are themselves determined by the process being characterized.

Therefore, according to Eq. (29), in this work the injection volumetric efficiency has been evaluated as:

$$\eta_{v,inj} = \frac{m_{inj}}{\left(\rho_{inj} - \rho_s\right) V_{dis}} . \tag{32}$$

With this new definition, once the injection volumetric efficiency is mapped, the injected mass can be easily assessed, since the denominator is known once the thermodynamic states representing the fluid at injection and suction are known.

An additional parameter, the *supercharging coefficient* χ, can be introduced to specifically quantify the supercharging effect provided by the vapor injection process. In this work, this parameter has been defined as follows:

$$\chi = m_{d,VI}/m_{d,ref} \tag{33}$$

where $m_{d,VI}$ represents the mass discharged in the vapor injection configuration, while $m_{d,ref}$ refers to the mass discharged by a compressor without vapor injection (equal to $m_{d,ref} = \eta_{v,ref}\rho_s V_{dis}$). Finally, the ratio of mass discharged by the compressor m_d to the ideal suction mass $\rho_s V_{dis}$ can be defined as the *mass discharge coefficient* $\lambda_{v,d}$, which is the product of the suction volumetric efficiency and the supercharging coefficient:

$$\lambda_{v,d} = \frac{m_{d,VI}}{\rho_s V_{dis}} = \eta_{v,ref}\chi . \tag{34}$$

Since χ is greater than one due to the supercharging effect provided by vapor injection, the mass discharge coefficient can also exceed unity (and for this reason it has not been labeled as efficiency).

Concerning the isentropic efficiency, it can still be defined using its conventional formulation; however, the reference power used in the calculation must be properly adjusted to account for the mixing effect introduced by vapor injection. An approach is the two-stage compression, which divides the entire compression process into two distinct phases, with the mixing occurring at the end of the first phase [37]. Another method involves parallel compression [38]: the main compressor handles the working fluid from suction to discharge pressure, while an auxiliary compressor operates between the injection and discharge pressures. The two possible approaches are illustrated in Fig. 2. Both definitions describe *idealized reference processes* used solely to evaluate the isentropic efficiency, and not the actual thermodynamic process taking place inside the cylinder, which is captured by the lumped-parameter model described in Section 2.1. In particular, in Eqs. (35)–(37) the symbol p_{inj} denotes the upstream injection-line pressure (i.e., the flash-tank pressure in the FTVI configuration of Fig. 1(b)), and the mixing in the two-stage reference is assumed to occur at constant pressure $p_{mix} = p_{inj}$. In the real compressor, the injected vapor experiences a pressure drop across the injection valve and mixes with the in-cylinder fluid at the variable cylinder pressure, which is lower than p_{inj}; these irreversibilities, together with heat transfer between the working fluid and the cylinder walls and leakage through the piston–cylinder clearance, are precisely the dissipative phenomena that cause η_{is} to be less than unity.

Table 3
Parameters required by the different definitions of the injection volumetric efficiency according to Lambers [38].

ID	Mass		Volume	
	Variable	Description	Variable	Description
A	$m_{s,ref}$	Drawn mass without injection	$V_{start,inj}$	Volume at start of injection
B	$m_{s,ref}$	Drawn mass without injection	$V_{end,inj}$	Volume at end of injection
C	$m_{s,inj}$	Drawn mass with injection	$V_{start,inj}$	Volume at start of injection
D	$m_{s,inj}$	Drawn mass with injection	$V_{end,inj}$	Volume at end of injection

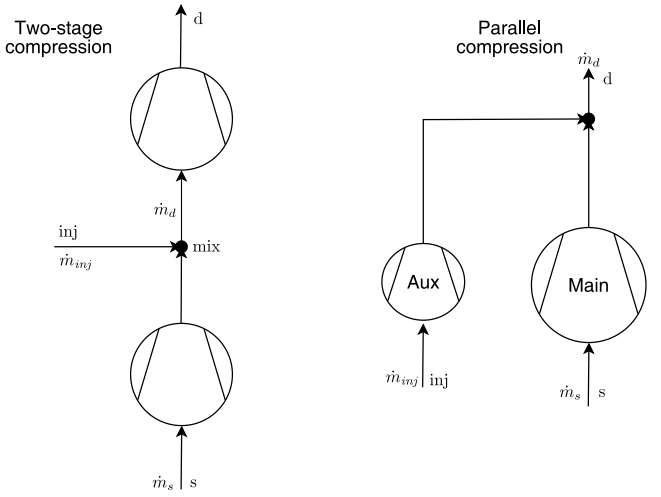

Fig. 2. Idealized reference processes for the definition of isentropic efficiency: two-stage compression with constant-pressure mixing at p_{inj} (left) and parallel compression (right). These are reference benchmarks used in Eqs. (35) and (38), not the actual in-cylinder process simulated by the lumped-parameter model.

Depending on the chosen approach, the reference power and therefore the isentropic efficiency can be evaluated as follows. Eq. (35) applies when two series compression processes are considered:

$$P_{id,series} = \dot{m}_s \left[h(p_{inj}, s_s) - h_s\right] + (\dot{m}_{inj} + \dot{m}_s) \left[h(p_d, s_{mix}) - h_{mix}\right] , \quad (35)$$

where $h(p_{inj}, s_s)$ represents the enthalpy at the intermediate pressure assuming an isentropic compression starting from the suction pressure p_s, $h(p_d, s_{mix})$ is the enthalpy at the compressor discharge pressure based on an isentropic compression starting from the intermediate pressure $p_{mix} = p_{inj}$, and finally h_{mix} and s_{mix} denote the specific enthalpy and entropy after the mixing process:

$$h_{mix} = \left(m_s h_s + m_{inj} h_{inj}\right) / m_d \quad (36)$$

$$s_{mix} = s\left(p_{mix}, h_{mix}\right) . \quad (37)$$

On the other hand, the ideal power consumption in the parallel compression configuration is :

$$P_{id,parallel} = \dot{m}_s \left[h(p_d, s_s) - h_s\right] + \dot{m}_{inj} \left[h(p_d, s_{inj}) - h_{inj}\right] . \quad (38)$$

The isentropic efficiency, η_{is}, can thus be evaluated as:

$$\eta_{is} = P_{id,x} / P \quad (39)$$

where $P_{id,x}$ is the ideal power consumption in isentropic processes with series or parallel compression, given by Eq. (35) or (38), and P denotes the actual mechanical power consumption, as obtained from the simulation performed using the mathematical model described in the preceding section.

2.3. Model validation

The mathematical model was first validated against performance parameters available for a compressor without vapor injection; in particular, the reciprocating compressor for which experimental data were available is the CD6-1600-72H model [46], manufactured by the Italian company Dorin spa. The geometric and kinematic parameters of the reference compressor, together with the model inputs and outputs and the parameters to be identified, are summarized in Table 2; the volumetric efficiency and overall compressor efficiency are plotted against the overall pressure ratio $\beta = p_d / p_s$ in Fig. 3.

The overall compressor efficiency is the product of mechanical efficiency and isentropic efficiency:

$$\eta_c = \eta_m \eta_{is} \quad (40)$$

Since precise data on the trend of mechanical efficiency were not available, mechanical losses (due to friction on the piston ring, bearings, etc.) were considered constant for a given rotational speed and were evaluated based on a maximum mechanical efficiency of 0.97 for a mechanical power consumption of 120 kW, according to information provided by the manufacturer. Additionally, in order to estimate the real isentropic efficiency, an electric motor efficiency of 0.9 was adopted, again based on the manufacturer's indications. The clearance ratio, the equivalent cylinder–piston clearance, and the flow coefficients of both the discharge and suction valves are required by the lumped-parameter mathematical model but are not directly available from the compressor specifications. Therefore, a multi-objective analysis was performed to estimate these parameters in order to achieve results consistent with the available experimental data, minimizing the error on the evaluation of isentropic and volumetric efficiency. Model results were compared with the experimental data in the operating conditions reported in Table 4. The model parameters to be identified were varied in a range defined in Table 5; the range of clearance volume ratio, equivalent cylinder–piston gap, and flow coefficients were constrained to ensure physically feasible values according to the information provided by the manufacturer.

The optimization aimed to simultaneously minimize the deviations between the simulated and experimental values of isentropic efficiency and volumetric efficiency. The problem was formulated as a weighted multi-objective optimization, with a weight of 0.65 assigned to volumetric efficiency and 0.35 to isentropic efficiency. More weight is given to the volumetric efficiency because the experimental isentropic efficiency is estimated according to the assumptions on mechanical efficiency and electric motor efficiency stated above. The problem was solved using the Pareto-based solver `paretosearch` implemented in MATLAB. By exploring the Pareto front, this approach enabled the identification of parameter values that best reconcile discrepancies across both efficiency metrics; the results are presented and discussed in Section 3.1.

Once the model was validated, the identified parameters—clearance ratio, the equivalent cylinder–piston gap and valve flow coefficients—were employed to predict the performance of a next-generation compressor with vapor injection (CD8-3000-150H), scaled up with respect to the CD6-1600-72H model and equipped with an injector valve. These parameters were carried over unchanged to the simulation of the new compressor, for the following reasons: the valve flow coefficients μ_s and μ_d are approximately invariant across geometrically similar designs and are therefore expected to transfer between members of the same compressor family; the clearance ratio ζ is set by design and is not expected to vary systematically with compressor size within the same

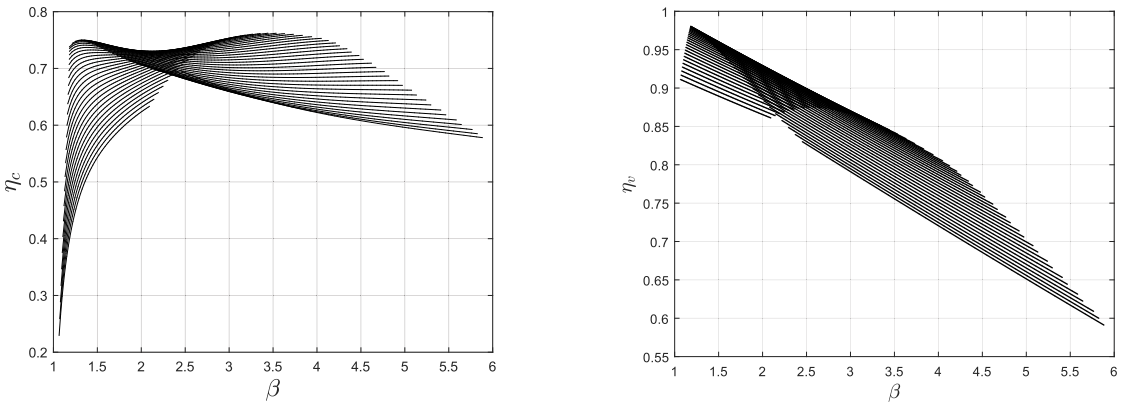

(a) Overall compressor efficiency (b) Volumetric efficiency

Fig. 3. CD6-1600-72H compressor performance.

Table 4
Operating conditions considered for model validation.

T_{ev}/°C	p_d/MPa
−5;0;5;10;15	8;9;10;11;12

Table 5
Range of values considered for the parameters identified with the model validation.

Parameter	Range
ζ	2–5 %
μ_s	0.45–0.65
μ_d	0.45–0.65
g	1–10 μm

Table 6
Input variable ranges used for ANN training and normalization.

p_d/MPa	β_{inj}	T_{ev}/°C	$\Delta\theta_{inj}$/°
8–15	1.05–1.7	−20–5	25–40

Table 7
ANN performance metrics across training, validation, and test subsets.

Subset	R	R^2
Training	0.99997	0.99994
Validation	0.99996	0.99992
Test	0.99996	0.99992
Overall	**0.99997**	**0.99994**
Best Validation MSE		3.9456×10^{-6}
Best Validation RMSE		1.99×10^{-3}

product family; and the equivalent cylinder–piston gap g is governed by manufacturing tolerance and sealing practice, which are common to the design family, rather than being a quantity that scales with bore or displacement. Since the CD8-3000-150H is a next-generation design currently under development and not yet available for testing, the corresponding results are presented as model-based predictions; the model structure is unchanged between the two compressors, so that these parameters can be re-identified directly against experimental data once a prototype becomes available, without any modification to the model. The geometric and kinematic parameters of this new compressor design are presented in Table 2 alongside those of the compressor used to validate the model.

2.4. Artificial neural network

To quickly predict reciprocating compressor performance under a wide range of operating conditions, an artificial neural network was developed using a fully connected neural network for supervised learning. The architecture is composed of an input layer, one or several hidden layers, and an output layer [47]. Each neuron performs a linear transformation which involves a weight matrix and a bias vector, which are learned during training, followed by a non-linear activation function. For a given input vector x, the linear transformation at each layer can be expressed as:

$$z^{(l)} = Z^{(l)}\phi^{(l-1)} + w^{(l)} \tag{41}$$

where $Z^{(l)}$ denotes the weight matrix, $w^{(l)}$ the bias vector, and $\phi^{(l-1)}$ the activation function from the previous layer. Before training, all input and output variables were normalized to the 0–1 range to enhance numerical stability and accelerate convergence:

$$x_{\text{norm}} = \frac{x - \min(x)}{\max(x) - \min(x)}\,. \tag{42}$$

This preprocessing step is critical in ANN training, as it ensures a consistent scale across features and mitigates the influence of varying magnitudes, thus improving convergence behavior and overall training stability. The input ranges used for normalization are summarized in Table 6.

The fully connected neural network was trained using the MATLAB *Neural Net Fitting* toolbox, which provides a convenient environment for constructing and training shallow networks. The toolbox supports a single hidden layer; this is not restrictive for the present application, since the mapping from operating conditions to compressor performance indicators produced by the lumped-parameter model is smooth and well-behaved, and is reproduced by a single-hidden-layer network with an overall coefficient of determination of 0.999 94 (Table 7). A deeper architecture would increase the number of parameters and the training and evaluation cost without a meaningful improvement in an approximation that is already accurate to four significant figures.

A total of 1920 data points per output parameter were used to train, validate, and test the network, with the dataset partitioned into training (70 %), validation (15 %), and test (15 %) subsets. The Levenberg–Marquardt backpropagation algorithm (`trainlm`) was employed as the optimizer, and early stopping based on validation performance was applied to prevent overfitting. A preliminary sensitivity analysis was performed to determine the optimal number of neurons for the single hidden layer, revealing that the best architecture consisted of a single

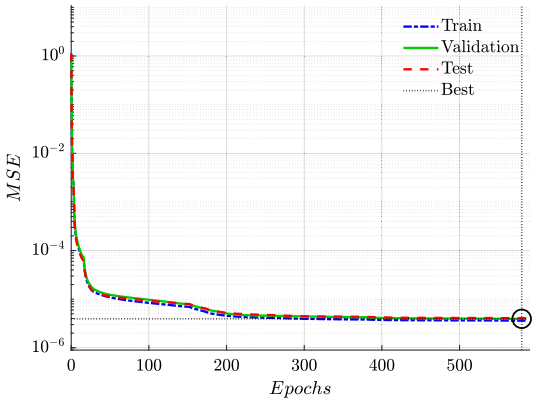

(a) MSE.

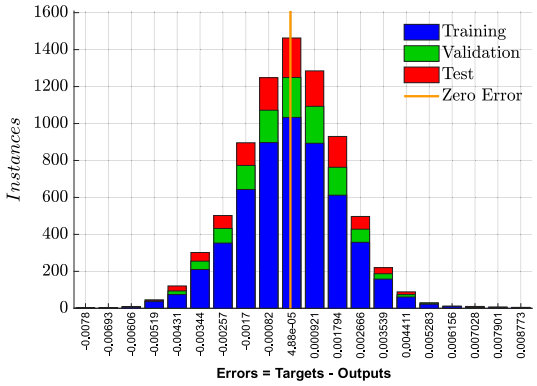

(b) Error histogram

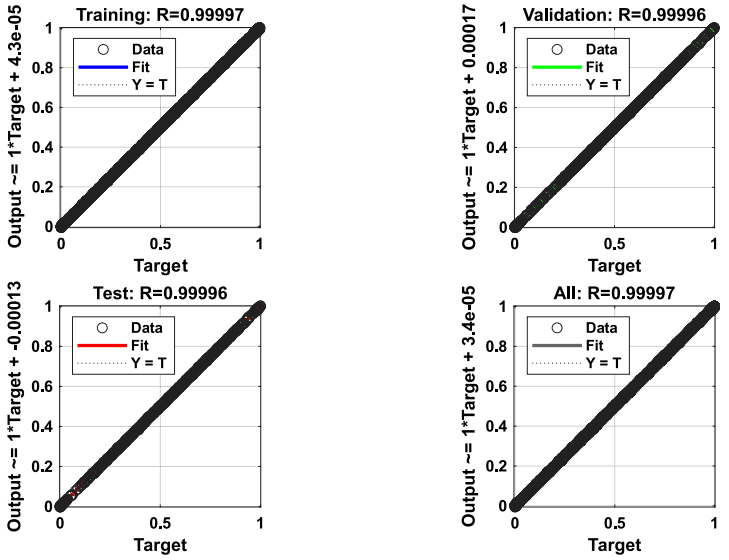

(c) Parity plot

Fig. 4. ANN training.

hidden layer containing 15 neurons, providing a well-balanced trade-off between model complexity, computational cost, and prediction accuracy. Once trained, the ANN enabled rapid estimation of key performance indicators (isentropic efficiency, volumetric efficiency, and specific work), thereby significantly reducing the computational time required for large-scale parametric analyses. The Levenberg–Marquardt algorithm converged in 586 epochs, achieving a best validation mean square error (MSE) of 3.9456×10^{-6} at epoch 580, as illustrated in Fig. 4(a). The predictive performance was assessed through the coefficient of determination (R^2) and the Root Mean Squared Error (RMSE). As shown in Fig. 4(c), the parity plot confirms excellent agreement between network predictions and target values across all subsets, yielding R^2 values of 0.99994, 0.99992, and 0.99992 for the training, validation, and test sets, respectively, with an overall $R^2 = 0.99994$ and an RMSE of 1.99×10^{-3}. These results are summarized in Table 7. Furthermore, the error histogram in Fig. 4(b) exhibits a symmetric, approximately Gaussian distribution of residuals centered near zero, with errors confined within the range -7.8×10^{-3}–8.8×10^{-3}, confirming that the model produces small, unbiased, and randomly distributed prediction errors consistent with a well-generalized regression model.

In addition, the neural network developed in this study has been used to assess the compressor performance over a wider range of operating conditions compared to those used to validate the model, and the results are presented in Section 3.3. The ANN will also be used in future works to implement the dynamic FTVI model in the Simulink/Simscape environment for control system design. In this regard, a Simscape component of a reciprocating compressor equipped with an injection valve was customized by integrating the previously described ANN (Fig. 5); this component is connected to the system through the suction, injection, and discharge ports, and implements the following constitutive equations, which determine the mass flow rates, the thermodynamic state at the compressor exit, and the mechanical power required by the compressor, once the pressure in the three branches connected to the compressor are known together with the injection valve opening time $\Delta\theta_{inj}$:

$$\dot{m}_s = \eta_{v,s}(p_s, p_{inj}, p_d, \Delta\theta_{inj})\rho_s V_{dis} n \tag{43}$$

$$\dot{m}_{inj} = \eta_{v,inj}(p_s, p_{inj}, p_d, \Delta\theta_{inj})(\rho_{inj} - \rho_s) V_{dis} n \tag{44}$$

$$\dot{m}_d = \dot{m}_s + \dot{m}_{inj} \tag{45}$$

$$h_d = h_d(p_s, p_{inj}, p_d, \Delta\theta_{inj}) \tag{46}$$

$$P = P(p_s, p_{inj}, p_d, \Delta\theta_{inj}). \tag{47}$$

3. Results and discussion

3.1. Reciprocating compressor model validation

As mentioned in Section 2.3, the calibration of the compressor model was carried out minimizing the discrepancy between the simulated and experimental volumetric efficiency (η_v) and the isentropic

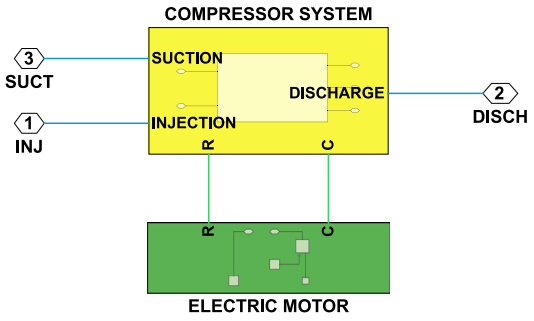

Fig. 5. Reciprocating compressor equipped with injection valve customized in Simulink/Simscape environment.

Table 8
Best parameters obtained.

ζ	g	μ_s	μ_d
2.8 %	1 µm	0.65	0.65

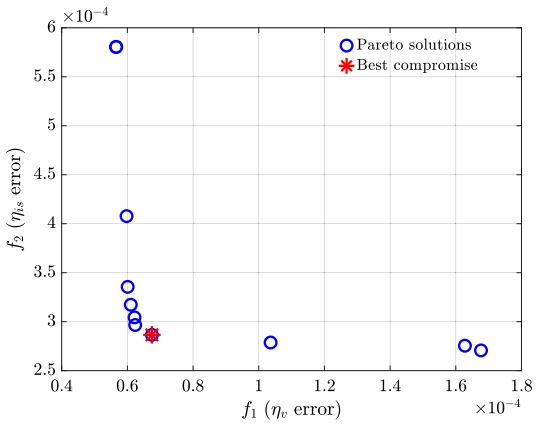

Fig. 6. Pareto front of the multi-objective parameter identification. Each point is a non-dominated parameter set; the axes report the MSE of the volumetric efficiency (abscissa) and of the isentropic efficiency (ordinate) over all operating conditions. The selected best-compromise solution, obtained by minimizing the weighted Euclidean distance from the origin (volumetric efficiency weight 0.65, isentropic efficiency weight 0.35), is highlighted.

efficiency (η_{is}) under all available operating conditions. The experimental data were obtained by the manufacturer from tests carried out in accordance with the standard UNI EN 13771-1. The corresponding measurement uncertainties, guaranteed between periodic instrument calibrations, are ±1 % on absolute pressure, ±1 % on absorbed power, ±1 % on mass flow rate, and ±0.3 K on temperature. From these figures, the relative uncertainty on the experimental volumetric efficiency can be estimated by propagation: since the volumetric efficiency is the ratio of the measured mass flow rate to the product of suction density, displacement and rotational speed, and the suction density depends on the measured pressure and temperature, its relative uncertainty is the quadrature sum of the relative uncertainties of mass flow rate, pressure and temperature (the temperature contribution being evaluated through the sensitivity of density to temperature). Taking the displacement and rotational speed as exact, this yields a relative uncertainty on the experimental volumetric efficiency of approximately ±1.4 % across the operating envelope, the value being governed almost entirely by the mass-flow and pressure accuracies, with a negligible temperature contribution. It should be noted that the experimental isentropic efficiency additionally depends on the assumed electric motor efficiency discussed in Section 2.3, which is based on qualitative information from the manufacturer and is not derived from direct measurement; a corresponding propagated uncertainty therefore cannot be quantified rigorously for the isentropic efficiency, and this is the reason a higher weight was assigned to volumetric efficiency than to isentropic efficiency in the validation procedure, as discussed in the following paragraphs.

For each candidate parameter set, the discrepancy between the simulated and experimental efficiencies was quantified as the mean square error of the volumetric and of the isentropic efficiencies over the full set of operating conditions. The best trade-off solution was then selected by minimizing the weighted Euclidean distance from the origin in the plane of these two error metrics, yielding the globally optimal parameter set used in the remainder of this work.

The Pareto front obtained from the multi-objective optimization is illustrated in Fig. 6, where each point represents a non-dominated solution in terms of the trade-off between the weighted volumetric efficiency error (65% weight) and the weighted isentropic efficiency error (35% weight). Each solution on the front is Pareto-optimal in the sense that no improvement in one objective can be achieved without a corresponding deterioration in the other, thereby providing a complete and unbiased representation of the conflict between the two fitting criteria across the explored parameter space. The best-compromise solution is highlighted distinctly on the front and corresponds to the parameter set that simultaneously achieves the most balanced reduction of both efficiency errors under the prescribed priority weighting. The best combination of parameters is reported in Table 8. The volumetric efficiency and isentropic efficiency predicted by the mathematical model using this set of parameters are compared with the experimental data in Fig. 7, which also includes the corresponding overall relative errors. As can be seen, the error in volumetric efficiency is consistently lower than 3 %. This deviation is of the same order as the ±1.4 % experimental uncertainty on the volumetric efficiency estimated above, indicating that a substantial part of the residual discrepancy is attributable to measurement uncertainty rather than to model error, so that the reported value represents an upper bound on the actual model deviation in volumetric efficiency. The error in isentropic efficiency is slightly higher, reaching a maximum of 5.4 %. These differences are attributable to the weighted objective function adopted during the optimization procedure, in which a higher weight was assigned to volumetric efficiency (65 %) relative to isentropic efficiency (35 %), for the reason stated above. Overall, the errors in isentropic efficiency remain within an acceptable range, in line with the accuracy levels reported in the literature for similar reciprocating compressor models [26].

After the model was validated, the injection phase was activated to assess the KPIs for a VI compressor. A comparative example of the indicator diagram is presented in Fig. 8 to highlight the different work cycles of compressors operating with and without vapor injection. The injection valve cross-section results in a ratio $SR_{inj} = 0.077$ according to preliminary design indications; the solenoid valve flow coefficient μ_{inj} has been set to 0.6 as a conservative assumption, compared to the identified values of the suction and discharge flow coefficients.

3.2. Assessment of key performance indicators

This section presents the assessment of the key performance indicators introduced in Section 2.2: the suction volumetric efficiency $\eta_{v,s}$ (Eq. (28)), the injection volumetric efficiency $\eta_{v,inj}$ in the newly proposed formulation (Eq. (32)) as well as in the variants previously available in the literature (Table 3), the supercharging coefficient χ (Eq. (33)), the mass discharge coefficient $\lambda_{v,d}$ (Eq. (34)), and the isentropic efficiency η_{is} evaluated against the two reference processes of Fig. 2 (Eqs. (35) and (38)). For each indicator, the dependence on the overall pressure ratio β, the injection pressure ratio β_{inj}, the evaporating temperature T_{ev}, and where relevant the injection valve opening duration $\Delta\theta_{inj}$ is quantified over the operating envelope defined in Table 9. The performance of the vapor injection compressor is compared,

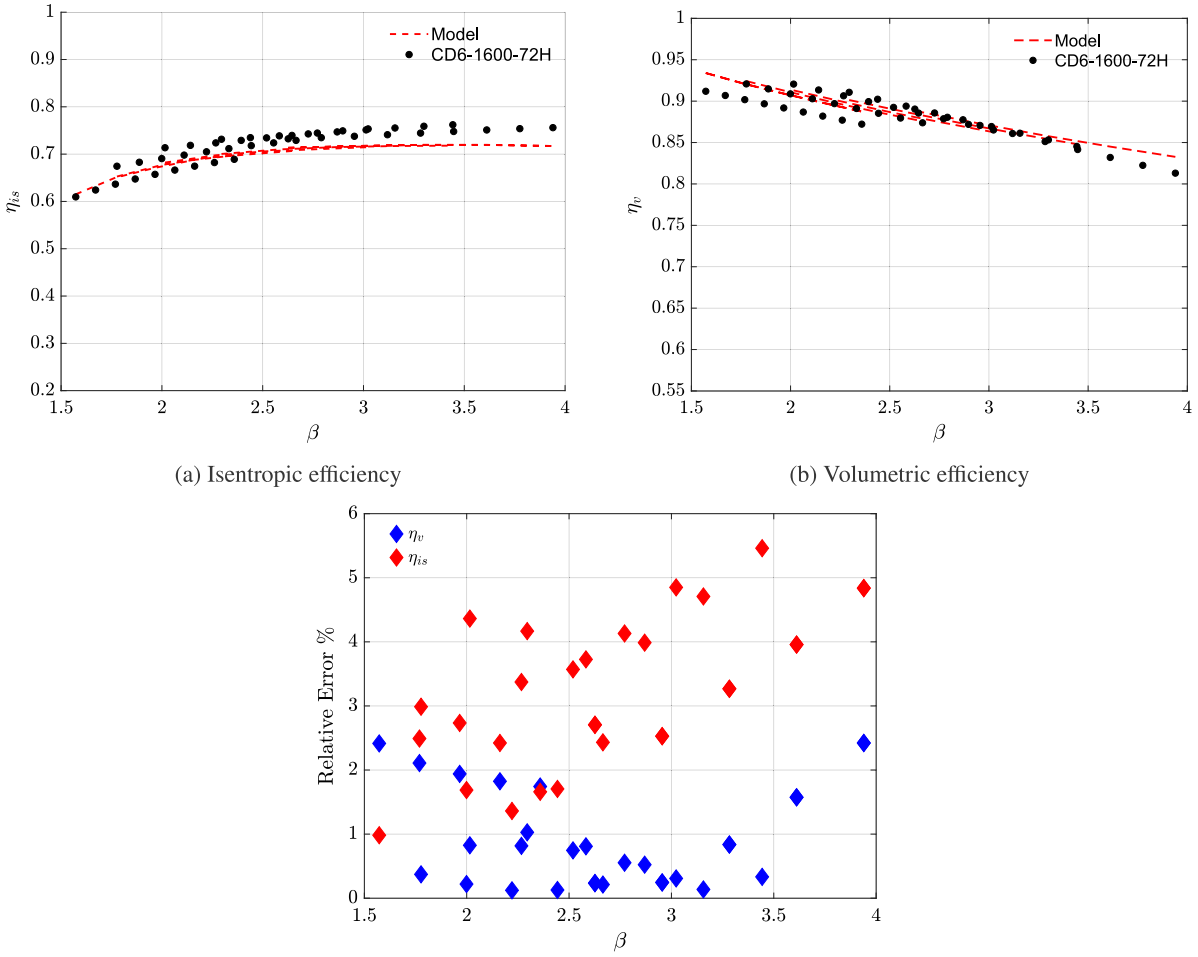

(a) Isentropic efficiency

(b) Volumetric efficiency

(c) Relative errors using the best parameters combination

Fig. 7. Comparison of efficiencies and relative errors with experimental data under different operating conditions.

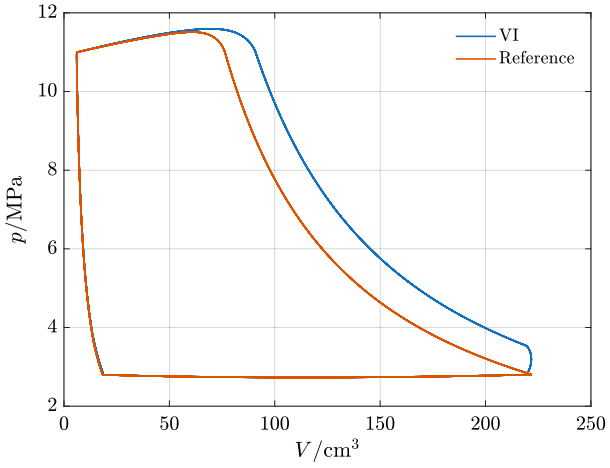

Fig. 8. Indicator diagram, $T_{ev} = -8\,°C$.

Table 9
Operating points considered to assess efficiencies.

T_{ev}/°C	p_d/MPa	$\beta_{inj} = p_{inj}/p_s$	$\Delta\theta_{inj}$/°
−20;−15;−10;−5;0;5	8;9;10;11;12	1.27 and 1.58	25

Table 10
Summary of compressor KPIs evaluated in this work, over the operating envelope of Table 9.

KPI	Range over envelope	Comparison with reference
$\eta_{v,s}$	0.76–0.92	reduced by 0.76–1.7 %
$\eta_{v,inj}$	0.20–0.85	VI-specific definition
χ	1.24–1.46	supercharging up to +45.7 %
$\lambda_{v,d}$	0.90–1.43	exceeds 1 over most of envelope
η_{is}	0.74–0.87	below reference (different ideal)
W	30–110 kJ/kg	reduced by 5.2–14.1 %

for each indicator, with that of the reference configuration without injection.

Fig. 9(a) illustrates the influence of vapor injection on suction volumetric efficiency $\eta_{v,s}$, evaluated using the operating points defined in Table 9. It is important to note that the duration of the injection was fixed at $\Delta\theta_{inj} = 25°$ (corresponding to 2.8 ms), which defines the minimum practical limit to implement vapor injection. In addition, two different ratios between injection and suction pressures, hereafter expressed as β_{inj}, were considered to analyze the influence of injection pressure on key performance indicators.

As shown, the compressor with vapor injection consistently has a lower suction volumetric efficiency compared to the reference case. This reduction is due to the interaction between the injection and suction processes around bottom dead center. When the injection valve opens, vapor at the injection pressure p_{inj}, which is higher than the in-cylinder pressure during suction, is admitted into the cylinder, locally

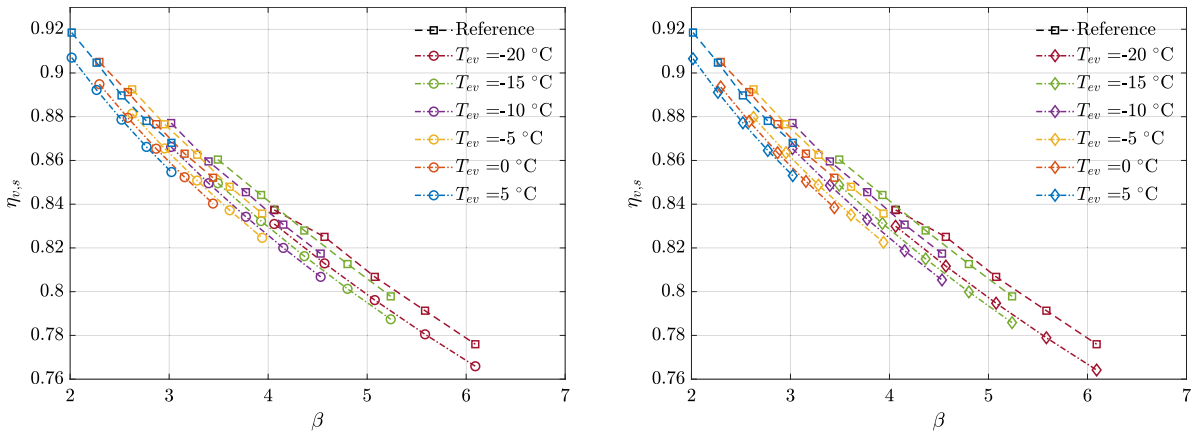

(a) $\beta_{inj} = 1.27$ (b) $\beta_{inj} = 1.58$

Fig. 9. Volumetric efficiency results according to Eq. (28).

raising the in-cylinder pressure and density. Since the suction valve is pressure-actuated and admits refrigerant only while the cylinder pressure remains below the suction-line pressure, the pressure rise produced by injection reduces the effective pressure difference driving the suction flow during the overlap interval, and thus the mass drawn through the suction valve. This interaction is visible in the indicator diagram of Fig. 8, where the VI cycle departs from the reference cycle in the region around bottom dead center. The extent of the interference nevertheless remains modest, because the injection duration ($\Delta\theta_{inj} = 25°$ in the cases analyzed) is short relative to the portion of the cycle over which suction takes place: in the analyzed cases, the reduction in the drawn mass due to vapor injection lies within a narrow range of approximately 0.76–1.54 % for $\beta_{inj} = 1.27$, and 0.9–1.7 % for $\beta_{inj} = 1.58$, relative to the reference configuration. The variation of this reduction across the operating envelope reflects the dependence of the overlap on the relative magnitude of the injected and drawn mass flows: at conditions where the injected mass is larger relative to the suction mass, the injection-induced pressure rise is more pronounced and the interference with the suction process correspondingly greater. Overall, vapor injection can be considered to have a rather limited impact on the suction process.

With respect to the total discharged mass, vapor injection obviously leads to an increase in mass flow. Although the drawn mass is reduced, the additional mass introduced through injection more than compensates for this reduction in all analyzed operating conditions, effectively producing a supercharging effect. The supercharging coefficient χ, illustrated in Fig. 10, is therefore always greater than one, according to the definition provided in Eq. (33). In the specific cases analyzed, the minimum increase in discharged mass is 24.1 %, occurring at an evaporating temperature of 5 °C. The maximum increase is 27.1 % for $\beta_{inj} = 1.27$ at −20 °C, and 45.7 % for $\beta_{inj} = 1.58$ at −5 °C. Finally, the mathematical model provides the basis for evaluating the operating conditions under which vapor injection becomes more advantageous for heat-pump operation, particularly in terms of the thermal power exchanged as a result of the supercharging effect.

Regarding the injection volumetric efficiency $\eta_{v,inj}$, when the approach proposed by Lambers [38] is considered (Table 3), its trend mirrors that of the classical volumetric efficiency, decreasing as the pressure ratio increases (Fig. 11(a)). Definitions A and B yield similar results, as do definitions C and D. This behavior primarily stems from the fact that definitions A and B consider the actual drawn mass without injection, whereas definitions C and D consider the actual drawn mass with injection. From simulations, it is known that the drawn mass in the reference configuration is higher than in the VI case. Thus, this represents the major difference. However, pairs A–B and C–D also present differences, although to a lesser extent. The reason lies in

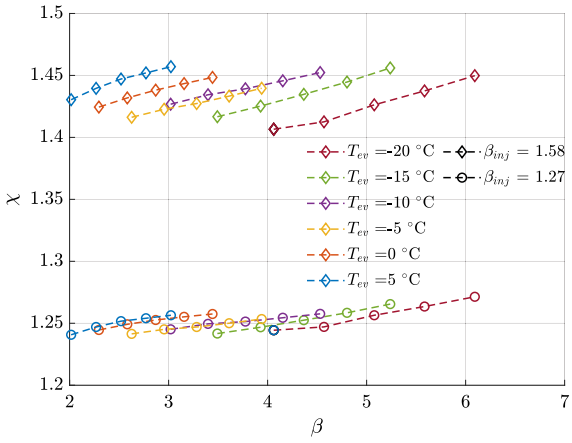

Fig. 10. Supercharging parameter.

the fact that in definition A the volume at the start of injection is considered, whereas in definition B the volume is evaluated at the end of injection. The same distinction applies to definitions C and D. Focusing on the definitions labeled A and C the percentage difference between the two curves ranges from 3.33 % to 4.8 %. In particular, Fig. 11(a) shows the results obtained with definition C.

In contrast, the definition of injection volumetric efficiency proposed by the authors, Eq. (32), produces values that are negligibly affected by the overall pressure ratio, as shown in Fig. 11(b). The pressure-ratio dependence of the Lambers definitions results in the injection volumetric efficiency changing by up to 19 %, whereas the dependence of the proposed definition is always lower than 0.8 % over the operating conditions analyzed in Fig. 11. This demonstrates that the proposed formulation is a more selective descriptor of the injection process: while the Lambers definitions conflate the effects of the injection and the overall compression ratio, the new definition decouples them, isolating the influence of the injection conditions alone. Therefore, this new definition is not only more practical, as discussed in Section 2.2, but also has the additional advantage of being almost exclusively dependent on suction and injection parameters, which are the properties that most affect the injection process. Fig. 11(b) shows that, while the injected mass increases with the injection pressure ratio β_{inj}, the injection volumetric efficiency decreases, due to the significant increase in the density difference $\rho_{inj} - \rho_s$ at the denominator; on the other hand, it increases with a decrease in suction pressure when the injection pressure ratio is kept constant, because the injected mass

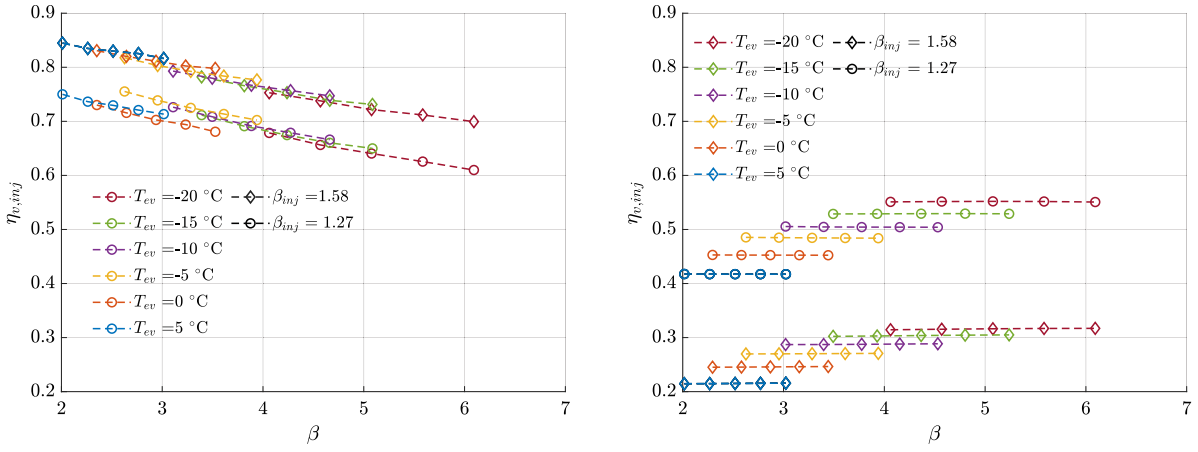

(a) According to Lambers, definition C in Table 3 (b) Newly introduced definition, Eq. (32)

Fig. 11. Injection volumetric efficiency.

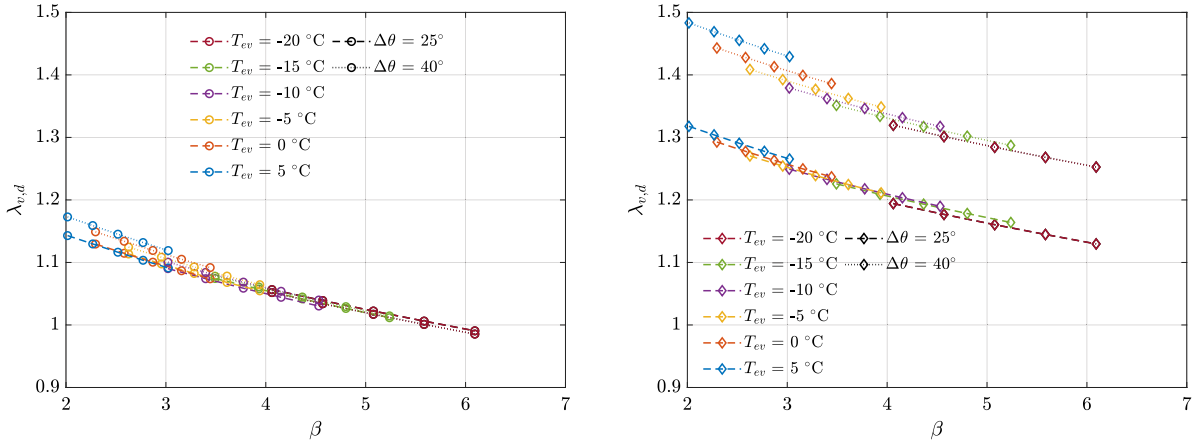

(a) $\beta_{inj} = 1.27$ (b) $\beta_{inj} = 1.58$

Fig. 12. Mass discharge coefficient.

changes only slightly while the density difference $\rho_{inj} - \rho_s$ increases significantly.

The mass discharge coefficient $\lambda_{v,d}$, defined by Eq. (34), is represented in Fig. 12. Since it is the product of the volumetric efficiency in the reference configuration without VI and the supercharging coefficient, it combines the most relevant features of both parameters, showing an almost linear decrease with the overall pressure ratio and a substantial increase with the injection pressure ratio. Fig. 12 also quantifies the effect of an increase in the duration of injection valve opening, which leads to a higher mass injected per cycle and therefore higher values of the mass discharge coefficient.

Attention is now directed to the evaluation of isentropic efficiency, which represents a key performance indicator for compressors. As described in Section 2.2, two alternative approaches were considered to define the reference power: in Fig. 13, round and diamond markers indicate the series compression being used as the reference, while cross markers denote parallel compression. A comparative analysis of the results indicates that the differences between these definitions are practically negligible. Specifically, the maximum percentage deviation observed is only 0.079 %, which occurs for a pressure ratio of 5.07 combined with an evaporating temperature of −20 °C. Consequently, it can be concluded that how the reference power is defined does not significantly influence the assessment of isentropic efficiency, and both formulations can be applied with confidence without affecting the reliability of the results. In Fig. 13, the isentropic efficiency of the VI compressor is compared to that of the reference compressor to show that similar qualitative trends are observed with respect to the overall pressure ratio. The isentropic efficiency is lower for the VI compressor, but this obviously does not mean that the power required is higher, as the ideal reference process is different in the two configurations: on the contrary, the specific work is significantly reduced by vapor injection as shown in the following section.

Table 10 summarizes the quantitative findings for each of the key performance indicators discussed in this section. Across the operating envelope considered, vapor injection produces a modest reduction in suction volumetric efficiency, a substantial supercharging effect with χ reaching +45.7 %, an injection volumetric efficiency that is nearly independent of the overall pressure ratio under the proposed definition (Eq. (32)), and a reduction in specific work of up to 14.1 % compared with the reference configuration without injection. The isentropic efficiency is slightly lower than in the reference case, but this reflects the different reference process used in its definition for the vapor injection configuration (Section 2.2) and does not imply higher power consumption.

3.3. Evaluation of specific work in VI and reference configuration

3.3.1. Compressor-level analysis

One of the main advantages of vapor injection is the reduction in the specific work required during the compression phase, as discussed

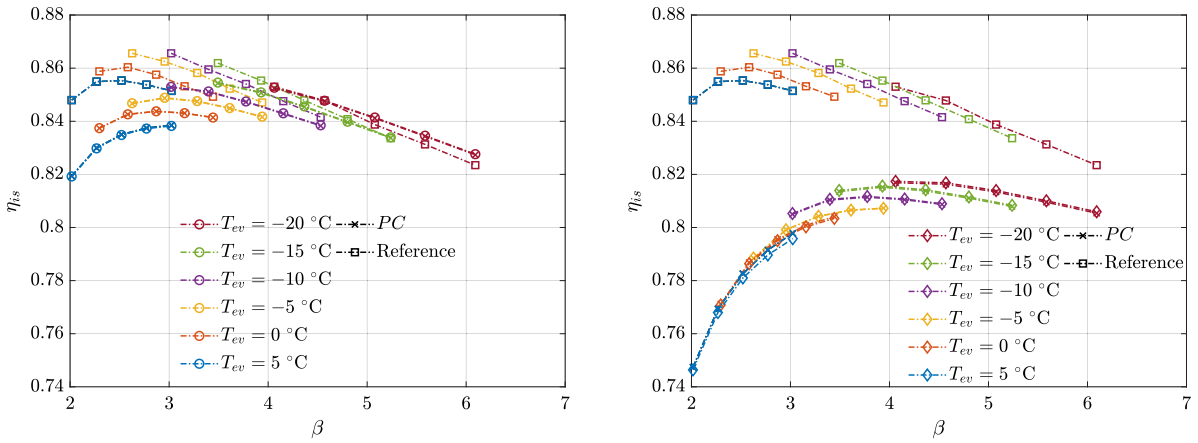

(a) $\beta_{inj} = 1.27$ (b) $\beta_{inj} = 1.58$

Fig. 13. Isentropic efficiency.

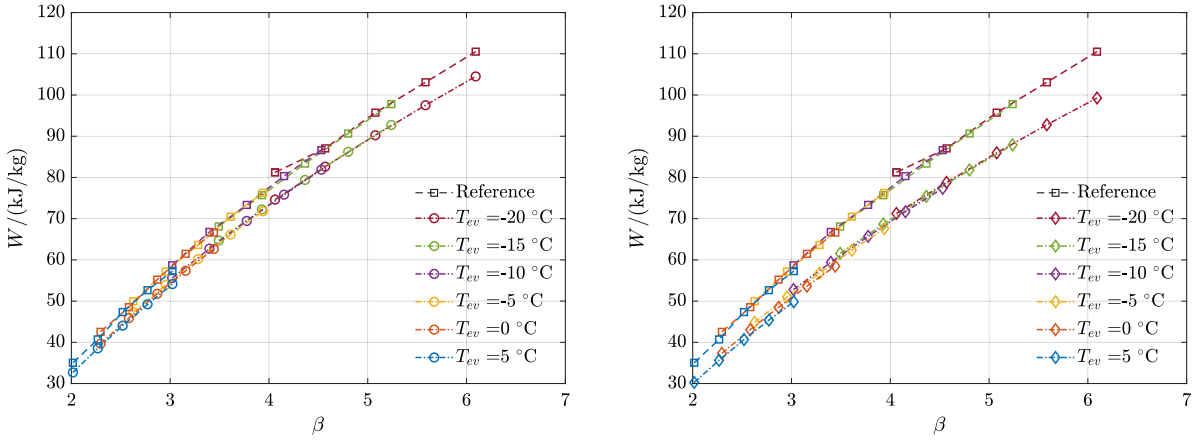

(a) $\beta_{inj} = 1.27$ (b) $\beta_{inj} = 1.58$

Fig. 14. Specific work comparison in VI and reference configuration.

in Section 1. This reduction originates from the multiple-effect principle introduced by Voorhees: the mass admitted through the injection valve enters the cylinder already at the intermediate pressure p_{inj} and is therefore compressed only from p_{inj} to the discharge pressure, whereas in the reference configuration the entire discharged mass is compressed from suction to discharge pressure. The work per unit discharged mass is consequently lower, since a fraction of the delivered mass bypasses the low-pressure part of the compression. In the indicator diagram of Fig. 8, this is reflected in the area enclosed by the VI cycle relative to the mass it discharges: although the injection of additional vapor modifies the in-cylinder pressure history, the increase in discharged mass more than compensates the change in work per cycle, so that the specific work is reduced with respect to the reference cycle.

The specific work calculated for the operating conditions summarized in Table 9 is presented in Fig. 14. The results obtained are consistent with those reported in the previous work of the authors [24], where a decrease in the evaporating temperature led to an increase in the specific work required. Moreover, as expected, the specific work required by the VI compressor is consistently lower than in the reference configuration.

The observed trends indicate that the ratio between the injection pressure and the suction pressure plays a crucial role in determining the specific work of the system. When a relatively low injection pressure ratio is considered, such as $\beta_{inj} = 1.27$, the influence of vapor injection is limited. As shown in Fig. 14(a), the minimum relative difference between the VI and reference configurations reaches 5.2 % for an evaporating temperature of 5 °C and an overall pressure ratio $\beta = 2.27$ (discharge pressure $p_d = 9$ MPa), while the maximum difference increases to 8.4 % for an evaporating temperature of −20 °C and a pressure ratio of 4.6 ($p_d = 9$ MPa). As a result, the performance improvement is modest, suggesting that, under these circumstances, the system does not fully benefit from the potential enhancement offered by the injection process. In contrast, when β_{inj} increases to 1.58, the impact of vapor injection becomes substantially more relevant. As shown in Fig. 14(b), the minimum and maximum differences between the VI and reference configurations increase to 9.26 % and 14.1 %, respectively. These values are observed at an evaporating temperature of −20 °C with $\beta = 3.93$, and at −5 °C with $\beta = 2.52$. The more pronounced decrease in specific work demonstrates that higher injection pressures substantially modify the compression process, yielding a more effective reduction in specific work.

3.3.2. System-level analysis: coupling between compressor and FTVI cycle

When the compressor is embedded in the FTVI cycle of Fig. 1(b), the injection pressure p_{inj} and the injection valve opening time $\Delta\theta_{inj}$, which were treated as independent operating parameters in the compressor-level analysis, become coupled through the steady-state mass balance at the flash tank. The coupling mechanism is expressed by Eq. (48), which equates the vapor quality produced by the flash expansion (set by p_{inj} and T_{gc}) to the ratio of injected mass to discharged mass (set

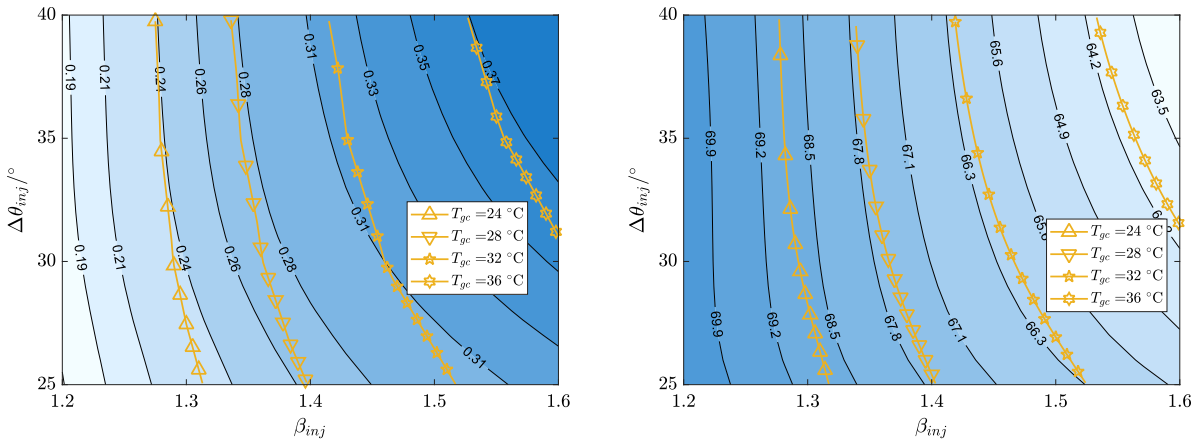

(a) m_{inj}/m_d (b) W/(kJ/kg)

Fig. 15. Performance of a VI compressor at fixed suction and discharge pressure ($T_{ev} = -10\,°C$; $p_d = 10\,MPa$). The yellow lines with markers represent graphically the constraint between injection pressure and injection valve opening time, expressed analytically by Eq. (48).

by the compressor model). This identifies a hierarchical optimization structure: at the compressor level, p_{inj} and $\Delta\theta_{inj}$ are jointly optimized to minimize specific work for a given pressure ratio; at the cycle level, the same pair of variables is constrained by Eq. (48), so that increasing one requires reducing the other, and the cycle-level optimum is then the constrained minimum of the compressor-level objective along the manifold defined by the constraint. The resulting trade-off, discussed in detail in the remainder of this subsection, is that the compressor-level optimum (high p_{inj}, long $\Delta\theta_{inj}$) is *not* attainable at the system level, where the optimum shifts to *low* p_{inj} and *long* $\Delta\theta_{inj}$, the configuration that maximizes the injected mass within the constraint imposed by the available flash-tank vapor quality.

For steady-state operation, the vapor quality in the flash tank, which depends on the enthalpy at the gas cooler exit and the injection pressure, must be equal to the ratio of injected mass to discharged mass (see Fig. 1(b)); the latter depends on the suction, injection and discharge pressure and on the injection valve opening time, according to the mathematical model presented in the previous sections, resulting in Eqs. (43)–(45). This steady-state constraint can thus be represented as follows:

$$q_{inj}(p_d, T_{gc}, p_{inj}) = m_{inj}/m_d = f(p_d, p_{inj}, p_s, \Delta\theta_{inj}), \tag{48}$$

and can be used to find the injection valve opening time that allows the injection of the vapor produced by the flash expansion, as a function of suction, injection, discharge pressure, and gas cooler exit temperature:

$$\Delta\theta_{inj} = \Delta\theta_{inj}(p_s, p_{inj}, p_d, T_{gc}). \tag{49}$$

An increase in injection pressure leads to a decrease in vapor quality in the flash tank and, hence, in the mass that can be injected into the compressor: as a result, given the values of suction and discharge pressure, the injection valve must be operated in such a way as to significantly reduce the opening time if the injection pressure is increased. Fig. 15 shows the behavior of the VI compressor for fixed values of evaporation temperature (which sets the suction pressure) and discharge pressure, resulting in an overall pressure ratio equal to 3.78, in terms of the ratio of injected to discharged mass (Fig. 15(a)) and the specific work (Fig. 15(b)) as functions of the injection pressure ratio and the injection valve opening time. These operating maps confirm the results presented in the previous sections: if the operation is not constrained by Eq. (48), an increase in injection valve opening time or injection pressure leads to a higher injected mass and, as a result, to a reduced specific work. However, the yellow curves in Fig. 15 show injection valve opening values that satisfy the constraint represented by Eq. (48), for different temperatures at the gas cooler exit: as the injection pressure increases, the injection valve opening must decrease rapidly to match the reduced availability of vapor produced in the flash tank. Consequently, once the operation of the entire system is considered, an increase in injection pressure does not lead to a lower specific work required by the VI compressor because of the reduction in the available vapor mass to be injected, confirming the results presented in the previous work in which the injection process was modeled with the assumption of constant-volume mixing [24]. These results are also illustrated by Fig. 16, which presents in a different way the data of Fig. 15(b) representing the specific work calculated by the compressor model when the constraint imposed by Eq. (48) is considered.

Fig. 16 also compares the results of the compressor model presented in this work with the predictions obtained under the constant-volume mixing assumption used in our previous work [24]. The constant-volume mixing process is selected here as the reference algebraic baseline for two reasons. First, it idealizes a limit — instantaneous mass injection with negligible cylinder volume change during the injection event — that is closer to the physical conditions of the present configuration than alternative idealizations such as constant-pressure or quasi-steady mixing, given the millisecond-scale opening durations of the solenoid-controlled injection valve. Second, all such time-independent algebraic mixing assumptions share the structural limitation that the injection valve opening duration $\Delta\theta_{inj}$ cannot enter the formulation as an independent operating variable, which would prevent its use as a control parameter both in the present system-level analysis and in the Simulink/Simscape control framework developed on top of the compressor model.

Under these premises, the constant-volume mixing assumption is found to overestimate the specific work predicted by the detailed compressor model by approximately 7–10.5 % across the operating envelope, depending mainly on the injection mass fraction and the gas cooler exit temperature, as illustrated in Fig. 16. The comparison reported in this figure confirms that the use of a time-resolved description of the injection event is necessary to obtain quantitatively reliable predictions of the specific work and to enable a meaningful coupling between compressor and cycle-level operation.

In summary, these results show that the injection process should be operated in such a way as to maximize the injected mass with an extended valve opening time and, counterintuitively, to reduce the injection pressure to increase the vapor quality in the flash tank. The authors are currently working on the design of a control system that sets the optimum operating conditions for heat pumps equipped with a VI reciprocating compressor.

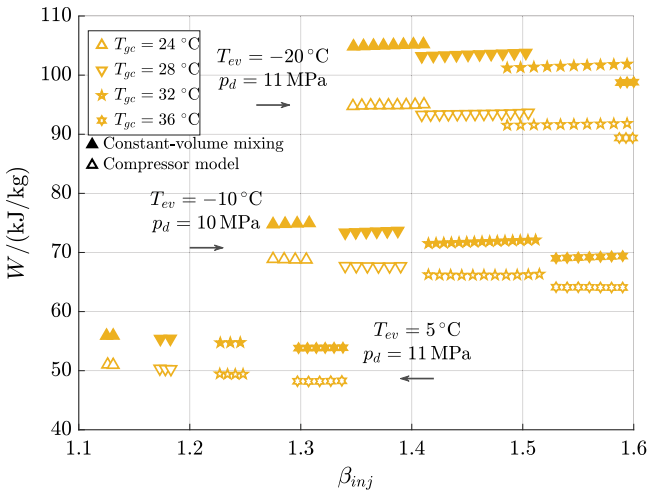

Fig. 16. Specific work comparison between the compressor model with the constraint set by Eq. (48) and the constant-volume mixing assumption for three distinct operating conditions.

4. Conclusions

This article presents a detailed mathematical model of a reciprocating compressor equipped with a vapor injection valve. The model incorporates kinematics, valve flow, and heat transfer to formulate two dimensionless differential equations representing mass and energy conservation, which allow the calculation of fluid properties within the cylinder over time, overcoming the simplifying constant-volume mixing assumption. The model was validated using experimental data from an existing compressor without vapor injection to identify the values of clearance ratio, valve flow coefficients, and effective cylinder–piston clearance. After validation, the model was used to assess key performance indicators of a reciprocating compressor equipped with a solenoid valve for vapor injection, including volumetric efficiency, isentropic efficiency, and specific work. In addition, a new indicator, defined as volumetric injection efficiency, $\eta_{v,inj}$, was introduced to specifically evaluate the vapor injection phase.

The most significant outcomes of the present analysis are highlighted in the following summary.

- Vapor injection entails a slight reduction in the drawn mass and, consequently, a decrease in suction volumetric efficiency, although within a limited range between 0.76–1.7 %.
- Vapor injection consistently ensures a supercharging effect, which becomes more pronounced as the ratio between injection and suction pressure increases. The supercharging coefficient slightly exceeds 45 %: under favorable operating conditions, the mass flow discharged by the VI compressor is significantly higher than in the reference configuration, increasing the heating capacity at system level.
- As reference ideal processes to assess isentropic efficiency, either a two-stage compression or a parallel compression can be considered without any noticeable difference in the final results.
- A reduction in specific work in the VI configuration is consistently observed compared to the reference configuration. This decrease depends not only on the discharge and suction pressures, but also on the injection pressure; for an injection pressure ratio of 1.58 and an injection valve opening time of 25°, the specific work can be reduced by up to 14.1 %.
- The injection pressure and the injection valve opening time, although independent at the compressor level, are coupled at the cycle level through the steady-state mass balance at the flash tank. This coupling defines a hierarchical optimization structure in which the cycle-level optimum is not the same as the compressor-level optimum: while the latter is obtained at high injection pressure and long valve opening time, the former is obtained at low injection pressure and long valve opening time, corresponding to the maximum injected mass available from the flash expansion.
- Finally, the constant-volume mixing assumption is shown to significantly overestimate the specific work required by the compressor, by 7–10.5 % over a wide range of operating conditions: therefore, the detailed compressor model presented in this work is necessary both to treat the injection valve opening duration as an operating variable and to estimate the compressor performance accurately.

The authors are currently working on implementing the FTVI scheme in a Simulink/Simscape environment, using the artificial neural network based on the mathematical model developed in this study, along with the results obtained in their previous work [24], to evaluate system performance indicators such as COP, including under off-design operating conditions. In addition, the authors aim to develop a control system for the vapor-injection phase, with the objective of optimizing control parameters, such as discharge pressure and valve opening time, to maximize the COP in off-design conditions.

CRediT authorship contribution statement

Luigi Fusco: Methodology, Software, Validation, Writing – original draft, Writing – review & editing, Visualization. **Giulio Lenzi:** Validation, Visualization. **Michele Manno:** Conceptualization, Methodology, Software, Validation, Writing – review & editing, Visualization, Supervision. **Stefano Mazzoni:** Software, Validation, Visualization.

Funding

This work was supported by the Ministry of Enterprises and Made in Italy, project n. F/350182/01-02/X60.

Declaration of competing interest

The authors declare that they have no known competing financial interests or personal relationships that could have appeared to influence the work reported in this paper.

Appendix. Nomenclature

a	constant value
A	heat transfer surface (m^2)
b	constant value
c	constant value
D	bore (m)
g	cylinder–piston clearance (μm)
h	specific enthalpy (J/kg)
l	variable cylinder height (m)
L	stroke (m)
m	mass (kg)
$\dot{m}$	mass flow rate (kg/s)
n	revolutions per second (rps)
N	number of cylinders

Nu	Nusselt number
p	pressure (MPa)
P	power (W)
Pr	Prandtl number
q	vapor quality
$\dot{Q}$	rate of heat transfer (W)
R	ratio of connecting rod length to crank radius
Re	Reynolds number
s	specific entropy (J/(kg K))
S	section (m^2)
SR	section ratio
t	time (s)
T	temperature (K)
u	specific internal energy (J/kg)
v	velocity (m/s)
V	compressor displacement (m^3)
W	specific work (J/kg)
$\dot{W}$	mechanical power (W)
Greek letters	
α	heat transfer coefficient (W/(m^2 K))
β	pressure ratio
ζ	clearance ratio
η	efficiency
θ	crank angle (rad, °)
λ	mass discharge coefficient
μ	flow coefficient valve
ρ	fluid density (kg/m^3)
χ	supercharging coefficient
ω	angular speed (rad/s)
Subscripts	
c	compressor
cyl	cylinder
$corr$	corrective
d	discharge
dis	displacement
ev	evaporator
f	fluid
gc	gas cooler
in	inlet (suction)
inj	related to vapor injection
is	isentropic
l	leakage
m	mechanical
mix	resulting from the constant-volume mixing process
out	outlet (discharge)
p	piston
ref	reference cycle
s	suction
v	volumetric
w	cylinder wall
Acronyms	
ANN	Artificial Neural Network
COP	Coefficient Of Performance
FT	Flash Tank
MSE	Mean Square Error
VI	Vapor Injection

Data availability

No data was used for the research described in the article.

References

[1] International Energy Agency, The Future of Heat Pumps, OECD, 2022, http://dx.doi.org/10.1787/2bd71107-en.

[2] A. Paez, B. Ballot-Miguet, B. Michel, P. Tobaly, R. Revellin, Experimental investigation of a new CO_2 refrigeration system arrangement for supermarket applications, Int. J. Refrig. 162 (2024) 245–256, http://dx.doi.org/10.1016/j.ijrefrig.2024.03.010.

[3] A. Arteconi, N. Hewitt, F. Polonara, Domestic demand-side management (DSM): Role of heat pumps and thermal energy storage (TES) systems, Appl. Therm. Eng. 51 (1) (2013) 155–165, http://dx.doi.org/10.1016/j.applthermaleng.2012.09.023.

[4] A. Hepbasli, A key review on exergetic analysis and assessment of renewable energy resources for a sustainable future, Renew. Sustain. Energy Rev. 12 (3) (2008) 593–661, http://dx.doi.org/10.1016/j.rser.2006.10.001.

[5] S. Pezzutto, D. Bottino-Leone, E. Wilczynski, R. Fraboni, Drivers and barriers in the adoption of green heating and cooling technologies: Policy and market implications for Europe, Sustainability 16 (16) (2024) 6921, http://dx.doi.org/10.3390/su16166921.

[6] United Nations, Amendment to the Montreal Protocol on Substances that Deplete the Ozone Layer, 2016, URL https://ozone.unep.org/treaties/montreal-protocol/amendments/kigali-amendment-2016-amendment-montreal-protocol-agreed.

[7] N. Abas, A.R. Kalair, N. Khan, A. Haider, Z. Saleem, M.S. Saleem, Natural and synthetic refrigerants, global warming: A review, Renew. Sustain. Energy Rev. 90 (2018) 557–569, http://dx.doi.org/10.1016/j.rser.2018.03.099.

[8] G. Lorentzen, J. Pettersen, A new, efficient and environmentally benign system for car air-conditioning, Int. J. Refrig. 16 (1) (1993) 4–12, http://dx.doi.org/10.1016/0140-7007(93)90014-Y.

[9] A. Zendehboudi, Thermo-economic evaluation of low-GWP CO_2-based zeotropic mixtures in space heating heat pumps with and without internal heat exchanger, Int. J. Refrig. 173 (2025) 1–17, http://dx.doi.org/10.1016/j.ijrefrig.2025.01.036.

[10] P. Nekså, CO_2 heat pump systems, Int. J. Refrig. 25 (4) (2002) 421–427, http://dx.doi.org/10.1016/S0140-7007(01)00033-0.

[11] D. Wu, B. Hu, R. Wang, Vapor compression heat pumps with pure low-GWP refrigerants, Renew. Sustain. Energy Rev. 138 (2021) 110571, http://dx.doi.org/10.1016/j.rser.2020.110571.

[12] M. Saikawa, S. Koyama, Thermodynamic analysis of vapor compression heat pump cycle for tap water heating and development of CO_2 heat pump water heater for residential use, Appl. Therm. Eng. 106 (2016) 1236–1243, http://dx.doi.org/10.1016/j.applthermaleng.2016.06.105.

[13] J. Stene, Residential CO_2 heat pump system for combined space heating and hot water heating, Int. J. Refrig. 28 (8) (2005) 1259–1265, http://dx.doi.org/10.1016/j.ijrefrig.2005.07.006.

[14] E.A. Groll, J.-H. Kim, Review of recent advances toward transcritical CO_2 cycle technology, HVAC&R Res. 13 (3) (2007) 499–520, http://dx.doi.org/10.1080/10789669.2007.10390968.

[15] K.J. Chua, S.K. Chou, W.M. Yang, Advances in heat pump systems: A review, Appl. Energy 87 (12) (2010) 3611–3624, http://dx.doi.org/10.1016/j.apenergy.2010.06.014.

[16] K.-M. Adamson, T.G. Walmsley, J.K. Carson, Q. Chen, F. Schlosser, L. Kong, D.J. Cleland, High-temperature and transcritical heat pump cycles and advancements: A review, Renew. Sustain. Energy Rev. 167 (2022) 112798, http://dx.doi.org/10.1016/j.rser.2022.112798.

[17] W. Li, B. Yue, H. Zhang, C. Zheng, P. Jiang, Y. Zhu, Optimization of transcritical CO_2 high-temperature heat pump cycle and study of maximum heating temperature, Int. J. Refrig. 177 (2025) 99–110, http://dx.doi.org/10.1016/j.ijrefrig.2025.05.023.

[18] C. Arpagaus, F. Bless, M. Uhlmann, J. Schiffmann, S.S. Bertsch, High temperature heat pumps: Market overview, state of the art, research status, refrigerants, and application potentials, Energy 152 (2018) 985–1010, http://dx.doi.org/10.1016/j.energy.2018.03.166.

[19] G.T. Voorhees, The Compression Refrigerating Machine, Nickerson & Collins co., 1927, URL https://babel.hathitrust.org/cgi/pt?id=uc1.$b663032.

[20] S. Zha, A. Hafner, P. Nekså, Investigation of R-744 Voorhees transcritical heat pump system, Int. J. Refrig. 31 (1) (2008) 16–22, http://dx.doi.org/10.1016/j.ijrefrig.2007.06.017.

[21] T. Morosuk, G. Tsatsaronis, C. Zhang, Conventional thermodynamic and advanced exergetic analysis of a refrigeration machine using a Voorhees' compression process, Energy Convers. Manage. 60 (2012) 143–151, http://dx.doi.org/10.1016/j.enconman.2012.02.021.

[22] K.J. Lambers, J. Süss, J. Köhler, Does the Voorhees-principle enhance the efficiency of CO_2 refrigeration systems? in: 7th IIR-Gustav Lorentzen Conference on Natural Working Fluids (GL2006), 2006, URL https://iifiir.org/en/fridoc/does-the-voorhees-principle-enhance-the-efficiency-of-co2-refrigeration-24456.

[23] K.J. Lambers, J. Süss, J. Köhler, Admission (economizer) port optimization of a Voorhees modified reciprocating CO_2 compressor, HVAC&R Res. 13 (3) (2007) 485–498, http://dx.doi.org/10.1080/10789669.2007.10390967.

[24] L. Fusco, M. Manno, S. Mazzoni, M. Vellini, Thermodynamic analysis of CO_2 transcritical cycles with vapor injection in reciprocating compressors (Voorhees cycles) for heat pumps operating at different design conditions, Int. J. Refrig. 180 (2025) 503–517, http://dx.doi.org/10.1016/j.ijrefrig.2025.09.016.

[25] C. Pérez-Segarra, J. Rigola, M. Sòria, A. Oliva, Detailed thermodynamic characterization of hermetic reciprocating compressors, Int. J. Refrig. 28 (4) (2005) 579–593, http://dx.doi.org/10.1016/j.ijrefrig.2004.09.014.

[26] E. Navarro, E. Granryd, J. Urchueguía, J. Corberán, A phenomenological model for analyzing reciprocating compressors, Int. J. Refrig. 30 (7) (2007) 1254–1265, http://dx.doi.org/10.1016/j.ijrefrig.2007.02.006.

[27] E. Winandy, C. Saavedra O, J. Lebrun, Simplified modelling of an open-type reciprocating compressor, Int. J. Therm. Sci. 41 (2) (2002) 183–192, http://dx.doi.org/10.1016/S1290-0729(01)01296-0.

[28] A. Cavallini, L. Doretti, G.A. Longo, L. Rossetto, B. Bella, A. Zannerio, Thermal analysis of a hermetic reciprocating compressor, in: International Compressor Engineering Conference, 1996, URL https://docs.lib.purdue.edu/icec/1160. Paper 1160.

[29] R.C. Chikurde, E. Longanathan, D.P. Dandekar, S. Manivasagam, Thermal mapping of hermetically sealed compressors using computational fluid dynamics technique, in: International Compressor Engineering Conference, 2002, URL https://docs.lib.purdue.edu/icec/1520. Paper 1520.

[30] M.L. Todescat, F. Fagotti, A.T. Prata, R.T.S. Ferreira, Thermal energy analysis in reciprocating hermetic compressors, in: International Compressor Engineering Conference, 1992, URL https://docs.lib.purdue.edu/icec/936. Paper 936.

[31] J. Rigola, N. Ablanque, C.D. Pérez-Segarra, A. Oliva, Numerical simulation and experimental validation of internal heat exchanger influence on CO_2 trans-critical cycle performance, Int. J. Refrig. 33 (4) (2010) 664–674, http://dx.doi.org/10.1016/j.ijrefrig.2009.12.030.

[32] R.P. Adair, E.B. Qvale, J.T. Pearson, Instantaneous heat transfer to the cylinder wall in reciprocating compressors, in: International Compressor Engineering Conference, 1972, URL https://docs.lib.purdue.edu/icec/86. Paper 86.

[33] W.J.D. Annand, Heat transfer in the cylinders of reciprocating internal combustion engines, Proc. Inst. Mech. Eng. 177 (1) (1963) 973–996, http://dx.doi.org/10.1243/PIME_PROC_1963_177_069_02.

[34] G. Woschni, A universally applicable equation for the instantaneous heat transfer coefficient in the internal combustion engine, 1967, http://dx.doi.org/10.4271/670931, URL https://www.sae.org/publications/technical-papers/content/670931/. SAE Technical Paper 670931.

[35] F.P. Disconzi, C.J. Deschamps, E.L.L. Pereira, Development of an in-cylinder heat transfer correlation for reciprocating compressors, in: International Compressor Engineering Conference, 2012, URL https://docs.lib.purdue.edu/icec/2103. Paper 2103.

[36] R. Aigner, H. Steinrück, Modelling fluid dynamics, heat transfer and valve dynamics in a reciprocating compressor, in: 5th EFRC Conference, 2007, pp. 171–180, URL https://repositum.tuwien.at/handle/20.500.12708/65538.

[37] F.M. Tello-Oquendo, E. Navarro-Peris, F. Barceló-Ruescas, J. Gonzálvez-Maciá, Semi-empirical model of scroll compressors and its extension to describe vapor-injection compressors. Model description and experimental validation, Int. J. Refrig. 106 (2019) 308–326, http://dx.doi.org/10.1016/j.ijrefrig.2019.06.031.

[38] K.J. Lambers, Isentropic and volumetric efficiencies for compressors with economizer port, in: International Compressor Engineering Conference, 2008, URL https://docs.lib.purdue.edu/icec/1920. Paper 1920.

[39] J. Tuhovcák, J. Hejčík, M. Jícha, Heat transfer analysis in the cylinder of reciprocating compressor, in: International Compressor Engineering Conference, 2016, URL https://docs.lib.purdue.edu/icec/2409. Paper 2409.

[40] S.K. Lohn, E.L.L. Pereira, Numerical investigation of the gas leakage through the piston-cylinder clearance of reciprocating compressors, in: International Compressor Engineering Conference, 2014, URL https://docs.lib.purdue.edu/icec/2295/. Paper 2295.

[41] V.M. Braga, C.J. Deschamps, Numerical analysis of gas leakage in the piston-cylinder clearance of reciprocating compressors considering compressibility effects, IOP Conf. Ser.: Mater. Sci. Eng. 232 (2017) 012006, http://dx.doi.org/10.1088/1757-899X/232/1/012006.

[42] R.T.S. Ferreira, D.E.B. Lilie, Evaluation of the leakage through the clearance between piston and cylinder in hermetic compressors, in: International Compressor Engineering Conference, 1984, URL https://docs.lib.purdue.edu/icec/424/. Paper 424.

[43] J. Zuk, P.J. Smith, Computer program for viscous, isothermal compressible flow across a sealing dam with small tilt angle., 1969, URL https://ntrs.nasa.gov/api/citations/19690023903/downloads/19690023903.pdf.

[44] L.R. Silva, C.J. Deschamps, Modeling of gas leakage through compressor valves, Int. J. Refrig. 53 (2015) 195–205, http://dx.doi.org/10.1016/j.ijrefrig.2014.05.003.

[45] M.E. Hosea, L.F. Shampine, Analysis and implementation of TR-BDF2, Appl. Numer. Math. 20 (1) (1996) 21–37, http://dx.doi.org/10.1016/0168-9274(95)00115-8.

[46] Dorin spa, CD6 1600-72H, 2025, URL https://dorin.com/it/catalogo/SE/CD/CD%20600/CD6%201600-72H/. Accessed 18 April 2025.

[47] R.B. Mahesh, J. Leandro, Q. Lin, Physics informed neural network for spatial-temporal flood forecasting, in: S. Kolathayar, A. Mondal, S.C. Chian (Eds.), in: Climate Change and Water Security. Lecture Notes in Civil Engineering, vol. 178, Springer, 2022, pp. 77–91, http://dx.doi.org/10.1007/978-981-16-5501-2_7.